2015

A numerical approach to the simulation of granular and multiphase flows

Ryan John Goetsch
Iowa State University

Recommended Citation

Goetsch, Ryan John, "A numerical approach to the simulation of granular and multiphase flows" (2015). *Graduate Theses and Dissertations*. 14416.
https://lib.dr.iastate.edu/etd/14416

A numerical approach to the simulation of granular and multiphase flows

by

Ryan John Goetsch

A thesis submitted to the graduate faculty
in partial fulfillment of the requirements for the degree of
MASTER OF SCIENCE

Major: Aerospace Engineering

Program of Study Committee:
Jonathan D. Regele, Major Professor
Alric Rothmayer
Thomas Ward

Iowa State University
Ames, Iowa
2015

TABLE OF CONTENTS

LIST OF TABLES

LIST OF FIGURES

ACKNOWLEDGEMENTS

This thesis would not have been possible without the support and guidance of many people. First and foremost, I would like to thank my advisor Dr. Jonathan Regele for his instrumental role in my journey. His expertise guided the direction of my work, while his patience allowed the freedom for me to think independently. Without his mentorship, I likely would not have chosen to pursue a graduate degree, and would have missed out on the rewarding experiences and personal growth that ensued.

I also owe my gratitude to the other members on my committee, Dr. Alric Rothmayer and Dr. Thomas Ward for their guidance and efforts in this work. In addition, I want to thank the members of my research group: Michael Kurtz, Zahra Hosseinzadeh-Nik, Mohamad Aslani, and Michael Phillips. I am grateful for their advice and friendship throughout my time at Iowa State University. Finally, my parents deserve special thanks for their enduring support and encouragement.

The computing equipment purchased through NSF MRI grant number CNS 1229081 and NSF CRI grant number 1205413 was also important in achieving the goals of this work.

ABSTRACT

Multiphase flows have been an active area of research for decades. Despite this, dense compressible gas-solid flows are still poorly understood. A experiment developed recently [Wagner *et al.*, Exp. Fluids **52**, 1507 (2012)] is able to isolate these conditions through the use of a multiphase shock tube. However, the behavior of the flow inside the particle curtain remains unclear. The objective of this work is to use numerical simulations to understand the fluid dynamics at the particle scale in this flow regime. An immersed boundary method is used to model the solid particles. The particles are tracked in the Lagrangian reference frame and collisions are modeled using the hard sphere approach. The fluid phase is solved on an adaptive grid using the Parallel Adaptive Wavelet-Collocation Method.

Detailed properties of the particle curtain are necessary for accurate simulations. Therefore, the discrete element method (DEM) is used to simulate the particle curtain in isolation. The model is first validated through comparison to a granular channel flow experiment. The mean and fluctuation velocity profiles are found to show good agreement. A fully three dimensional simulation of the particle curtain used by Wagner *et al.* yields information about the curtain's volume fraction and velocity profiles. The results suggest that the volume fraction profile is not uniform as previously thought.

CHAPTER 1. INTRODUCTION

1.1 Introduction

Multiphase flows are common and have important implications in many natural and industrial processes. Multiphase flows are considered to be any flow that consists of more than one phase, generally separated at scales larger than the molecular level. While many categories of these flows exist, the interest of this work is in gas-solid multiphase flows. In the natural world, these types of flows occur during sand storms, volcanoes, and avalanches. In industrial applications, this flow regime is observed in fluidized bed reactors and pneumatic conveyors, just to name a couple applications. The important economic implications in the design of industrial equipment that process these types of flows have driven research in better understanding and prediction of multiphase flows.

There have been relatively successful models developed that can simulate specific regimes of gas-solid multiphase flows. The most successful models are generally limited to flows where the solid phase is either dilute or densely-packed. In these extremes, simplifying assumptions can be made to ease the modeling efforts. However, these assumptions become invalid for flows in the intermediate regime, where the solid volume fraction is high, but not in a granular regime [4, 5]. Additionally, in regimes where complexities such as flows with high Reynolds numbers and situations where compressibility effects are important, modeling becomes increasingly difficult. Flows of these types are precisely the interest of this work.

These types of flows occur during volcano eruptions, where ash and rock fragments interact with the compression waves resulting from sudden explosions. These compressible, high Reynolds number flows are also present in the detonation of explosives when a shock wave passes through the cloud of solid particles as depicted in Fig. 1.1.

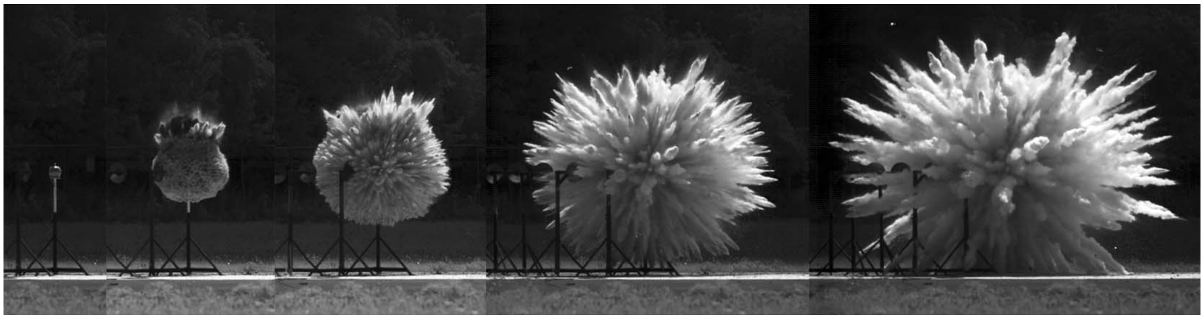

Figure 1.1 Photographs of a gas-solid multiphase flow occurring during an explosion [1].

There are many inherent difficulties encountered when trying to quantitatively measure flows in this regime experimentally. First of all, it is very difficult to isolate flows where the volume fraction lies in the dense, non-granular regime. For example, in the commonly studied fluidized bed reactor, while there are regions where the solid volume fraction is in this intermediate regime, there are also regions that are simultaneously in the dense, granular regime and other regions that the solid particles are dilute. Therefore, isolating only the intermediate volume fraction regions in these types of flows is problematic. The other main difficulty when studying gas-solid flows in this regime is probing the fluid properties. The flow features are often masked by the densely packed, opaque particles making measurements difficult.

These difficulties explain the significant gap in the experimental research that is crucial for furthering the understanding of this regime of flows. There have been some experiments that have looked at shock wave interactions with particle clouds. In the dusty regime, experiments have been performed [6], and drag coefficient models have been developed [7]. On the other extreme, where the particles are in a granular state, there have been studies focusing on shock interaction with a dense bed of particles [8]. However, research in the regime between these extremes has been lacking, leading to the necessity of extrapolating models from either extreme to predict properties in this dense, non-granular regime [9].

However, recent experimental work utilizing a multiphase shock tube shows promise in the quantitative measurement of these types of flows [2]. In this experiment, a gravity driven particle curtain allows the isolation of a high solid volume fraction multiphase region. This

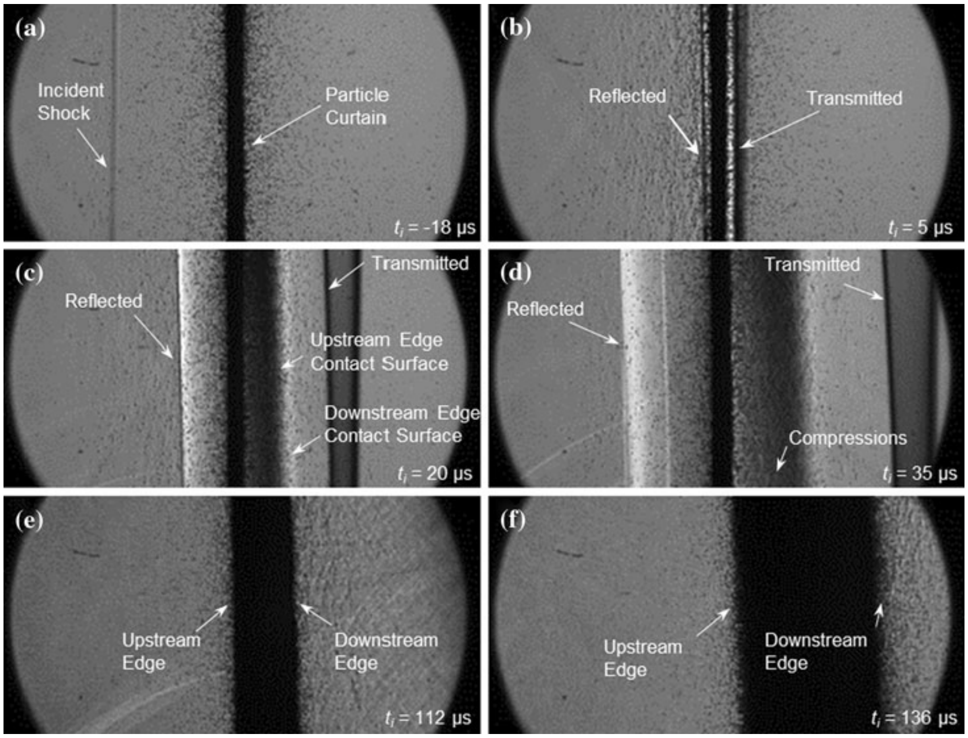

Figure 1.2 Schlieren images from a recent experiment studying the interaction between a shock wave and particle curtain [2].

curtain is mounted inside a shock tube, allowing study of the interaction between a shock wave and the particle curtain. Schlieren images, as shown in Fig. 1.2, are used to visualize the flow features that develop. In addition, pressure measurements allow quantitative data to be collected.

However, as mentioned above, the opaque nature of the particles makes it difficult to tell what is occurring at the particle scale inside and immediately behind the particle curtain. Additionally, detailed measurements such as the unsteady lift and drag forces experienced by the particles are not obtained, and are very difficult to measure in experiments. Many times, numerical simulations must be used in order to fully characterize these types of flows.

The advantage of numerical simulations is the ability to access any flow quantity at any location in the flow field, allowing detailed "measurements" to be taken. However, the simulation is only as accurate as the approximations made and the resolution used. Due to the wide range of scales present, great demands are placed on the numerical methods used to simulate these types of flows. In this largely uncharacterized regime of gas-solid flows, the luxury of under-resolving the flow features and using models for the sub-grid scales is not possible. However, detailed particle-resolved simulations can help to develop a more general model for these sub grid scales, allowing much larger industrial scale simulations to be possible.

This work details the application of the adaptive wavelet collocation method (AWCM) to the simulation of these types of flows. This method is an efficient grid adaptation method that allows highly resolved simulations while minimizing the total grid points necessary. When applied to gas-solid multiphase flows, the AWCM allows one to fully resolve flow features such as sock waves, boundary layers, and unsteady turbulence, while using less resolution in smooth regions of the flow.

This work also discusses granular simulations techniques used to model particle-particle interactions. Both hard sphere and soft sphere models are discussed. The hard sphere model is applied to the fully resolved multiphase simulation, while the soft sphere model is used to characterize the properties of the particle curtain which are necessary for the initial conditions.

1.2 Thesis organization

Chapter 2 is a paper that describes the equations and numerical methods used in the simulation of gas-solid multiphase flows. This includes the fluid phase governing equations and numerical methods, followed by the solid phase equations and methods. Then the coupling between phases is discussed, followed by some proof of concept results that showcase the abilities of this technique.

In chapter 3, the simulation of granular flows using the discrete element method (DEM) will be discussed. In this chapter, the particle curtain used in Ref. [2] is simulated and its properties are predicted and summarized. These properties are important for the initial conditions of a multiphase simulation of this experiment.

Finally, general conclusions will be drawn in chapter 4.

1.3 Literature review

1.3.1 Wavelet methods

Wavelets were first introduced by Grossmann and Morlet [10] and are typically used in applications ranging from image processing to speech recognition. Original “first generation” wavelets represent functions as a sum of a translations and dilations of a base wavelet at multiple levels of resolution. Wavelets have the property that they are localized in both physical and wavenumber spaces. Therefore, a sharp feature at one location has no effect on the wavelet transform far from it. This means that wavelets have the natural ability to compress information that contains localized features. Additionally, the existence of a fast wavelet transform has increased the usefulness of wavelet transforms for a variety of applications [11].

The use of wavelets in solving partial differential equations (PDEs) is a relatively recent application for the wavelet transform. Wavelets have been used in the solution of both linear [12] and non-linear PDEs [13, 14, 15, 16, 17, 18]. Additionally, they have shown great promise in the field of computational fluid dynamics (CFD) as summarized in Ref. [11].

The ability of wavelets to isolate localized features of a solution have made them useful in the simulation of turbulent fluid flow. Turbulent flows are characterized by their intermittent localized flow features. Typically, direct numerical simulation (DNS) of these flows requires a computational grid with enough resolution to capture all scales of these localized features down to the smallest (Kolmogorov) scale. However, by applying the wavelet transform to DNS methods, it allows fully resolving the highly transient and localized small scales at the highest resolution, while allowing a lower resolution grid to be used in smoother regions of the fluid. An example work that applied wavelet methods to DNS is Ref. [19].

Wavelet methods have also been applied to the large eddy simulation (LES) of turbulent flow [20]. The premise behind LES is that the smallest scales of turbulence are universal, and therefore do not need to be resolved. Instead, filtered equations are solved, and the under resolved small scales are modeled as a sub-grid stress term. The advantages of the wavelet transform that applied to DNS are also applicable to LES. The wavelet method allows resolving only the necessary regions of the flow while saving computational expense where high resolution is not needed.

Another area of CFD where wavelet methods have proven to be useful is in studying fluid-structure interactions. Immersed boundary methods have been applied with the wavelet method to allow resolved flow around solid obstacles [21, 22]. Once again, the wavelet method shines in its ability to fully resolve small scale flow features, such as the boundary layers in this case, while allowing computational savings in smoother regions of the solution.

In general, there are two different types of wavelet methods. The first is the adaptive wavelet Galerkin method (AWGM) and the other is the adaptive wavelet collocation method (AWCM). The AWGM solves the PDEs in wavelet coefficient space while the AWCM solves them on an adaptive grid in physical space [23]. The AWCM has the advantage of being much simpler to treat non-linearities in the equations in addition to general boundary conditions. Additionally, there are now so-called "second generation" wavelets that are used in this work. These wavelets remove the restriction mentioned above of all wavelets being translations and dilation of a base wavelet. By removing this restriction, it allows these wavelet methods to be used on general domains and have irregular sampling intervals [23].

1.3.2 Multiphase flow simulation

Over the decades that gas-solid multiphase flows have been actively studied, there has been a lot of effort expended in creating models to predict these types of flows. These models are based on the idea of modeling each phase separately and treat the interaction between the phases through various coupling methods. The various methods can be divided into three main categories based on how the solid phase is treated and the corresponding method for coupling the two phases. The categories differ based on the scale of flow features that are resolved. The methods that only resolve the larger scale flow features are generally able to handle larger scale problems, but are hindered by the accuracy of the models for the sub-grid flow features. On the other hand, the methods that resolve all features of the flow require very little modeling, but are limited by the high computational cost. A summary of the various methods can be found in Refs. [24, 25].

1.3.2.1 Two fluid models

At the lowest computational cost end of the modeling spectrum lies the two-fluid model for gas-solid multiphase flows [26]. These methods treat both the gas and solid phases as continua. This class of models requires modeling of the particle-particle collisions within the solid phase and coupling terms to model the drag forces that occur between phases.

Although this method is very useful for large scale problems due to its under-resolved nature, it is limited by the accuracy of the closure models for the solid phase stresses due to collisions and drag forces from the fluid acting on the solid phase. In cases of interest in this paper, where high Reynold's numbers and shock waves are present, these closures are not valid and therefore this method is not practical for the flows of interest.

1.3.2.2 Point particle models

The next level of resolution in modeling gas-solid flows can be classified as the point particle approach [27, 28, 29]. This approach differs from the previous in that each particle is tracked in the Lagrangian frame of reference. The collisions between particles are resolved using either hard sphere or soft sphere models as described below. Although modeling is still involved in predicting the collisions, this method is able to resolve the solid phase dynamics to a much greater level of detail compared to the continuum representation.

In the point-particle approach, the fluid phase is solved in much the same way as the two fluid approach. The governing gas equations are volume averaged, generally on a scale larger than the particle size. The inter-phase forces are computed using correlations given the particle and fluid velocities at the particle locations.

The equation for the motion of a spherical particle in a fluid is generally referred to as the BBO equation after Basset [30], Boussinesq [31], and Oseen [32]. A thorough derivation for a small particle in a non-uniform, unsteady, and low Reynolds number flow can be found in Ref. [33] and a summary of various correction terms can be found in Ref. [24]. For example, there are terms that have been developed to account for the effects due to undisturbed flow, steady state drag, compressibility effects, turbulence effects, particle clouds, virtual mass effect, Basset force, and lift forces. However, many of these empirical correlations have a very limited range of applicability. For example, when studying turbulent gas-solid flows, most drag correlations assume that the particle size is smaller than the smallest scale in the flow so that the flow in the vicinity of the particle, at the particle scale, is relatively laminar [34, 35].

Due to the volume averaged nature of the fluid solution, a relatively low resolution numerical grid is able to be used. The main limitation of this approach is the number of particles that can be feasibility tracked. With modern computers, this allows simulations of problems approaching industrial scales. However, due to many unknowns in the drag correlations for the compressible, high Reynolds number flows of interest, the point particle approach is not feasible for this work.

1.3.2.3 Particle resolved simulations

The class of techniques that require the least amount of modeling are those that resolve the particles in the fluid. These methods apply the no-slip boundary conditions at the particle surfaces directly. This allows direct calculation of the two-way coupling between the solid and fluid phases without the need for drag force closure models. Given sufficient resolution, these methods are applicable over the widest range of flow regimes.

There has been some interesting work that is an intermediate step between point-particle and particle resolved approaches in terms of modeling level and computational expense [36, 4, 37]. In these works, a coarse grid is used that is unable to resolve the flow features near the particles' surfaces. However, an analytical Stokes solution is extrapolated from the grid points in the fluid to the particles' surfaces. This allows a resolved analytic solution near the particles to calculate the fluid forces and enforce the boundary conditions, without needing to resolve the flow with a fine computational grid. However, the Stokes approximation must remain valid in the flow region immediately adjacent to the particles meaning generally that low to moderate Reynolds numbers are required.

Another approach to particle resolved gas-solid simulation utilizes body-fitted meshes that ensure grid points lie exactly on the particles' surfaces. For example in Ref. [38], the computational grid is re-meshed at every time step as the particles move. In that work, Reynolds number on the order of 100 are simulated, but due to the expense of re-meshing at every time step, these types of simulations are limited to small numbers of particles.

There have also been simulations that utilize immersed boundary methods. These methods eliminate the necessity for grid points to lie directly on the particle's surface. Instead, the fluid phase is solved everywhere (including inside the particles), but terms are added to the equations to enforce the boundary conditions at the particle surfaces. This technique has been employed to study heat transfer effects [39] and the effect of particles on turbulence [40].

The immersed boundary method provides the most promise in studying the flows of interest in this paper. In a recent work, the Brinkmann penalization method for immersed boundaries has been extended to allow any arbitrary Dirichlet, Neumann, or Robin-type boundary condition and works in compressible flows [21]. This technique does not require any modeling to compute the forces on the particles, as they can be computed directly from the fluid solution. In additoin, the immersed boundary method allows the use of a Cartesian grid, and therefore works well with the AWCM discussed above. Unlike in Refs. [39, 40], where a uniform grid is used for solving the fluid phase, the AWCM allows the computational grid to be refined in only the necessary areas such as the particle boundary layer and shock waves. This creates the ability to solve larger scale problems with the same amount of computational resources.

1.3.3 Granular flows

Another goal of this work is to predict the particle curtain properties in Ref. [2]. This prediction requires accurate simulation of granular flows. This section will provide a brief summary of the historical granular flow experimental work and modeling efforts.

1.3.3.1 Experimental investigation

Granular flows have been the subject of many experiments. Through these experiments, some general observations have emerged about granular flows. These flows are interesting because of their apparent simplicity, yet surprising complexity. For example, depending on the amount of external energy supplied to a granular system, these flows can exhibit properties ranging from solid-like to gas-like [41, 42]. Although the terminology may differ, generally, granular flows are broken into three regimes [43]. The first is known as the quasi-static regime where particle inertia can be neglected. In this regime soil plasticity models are often used to predict this type of flow [44, 45]. In the gaseous regime, binary collisions dominate and kinetic theory can be used [46, 47]. The intermediate regime where particles are still under a sustained network of contacts, but inertia effects become important is known as the dense flow regime [42].

The inelastic nature of granular flows means that they need to be continuously supplied with energy in order to obtain a steady state flow in the dense regime [48]. There are six types of flows that are generally studied experimentally due to their relative ease in creating this steady supply of energy [43]. These include plane shear flow, annular flow, vertical chute flow, flow over an inclined plane, heap flow, and rotating drums. Due to the similarity to the flow in the hopper region that feeds the particle curtain, the focus here will be on the vertical chute flow/hopper flow.

The collective experimental work on hopper flows have lead to the observation of some general characteristics of these types of flows. The first is the nature of the mean velocity profile within the hopper. These flows are generally characterized by a centralized plug flow region with shear layers near the walls. The shear layer thickess is found to scale with particle diameter regardless of the geometry of the channel [49, 50].

There has also been success in the development of an empirical correlation called the Beverloo equation that predicts the effect of the hopper geometry on the mass flow rate for a flat-bottomed hopper [51]. This relation has been extended for rectangular hoppers [52] and to account for angled side walls [53]. This relation has been validated through numerical simulations [52, 54] has proven to be relatively good at predicting this type of flow.

Another common observation is the pressure saturation at the bottom of a hopper filled with a granular material. Unlike a fluid, whose pressure monotonically increases with depth, in a granular flow it is observed that above a critical depth, the pressure at the bottom of the hopper becomes independent of the height of the particles above it [55].

1.3.3.2 Numerical modeling techniques

There are three main approaches used to model granular flows. The first is through the use of continuum models. This approach treats the granular material as a continuum material. However, as stated above, the dense regime between the gaseous and quasi-static regimes is not well understood, and therefore it has been difficult to develop constitutive relationships for flows in this regime [43]. Therefore, continuum approaches are limited in their usefulness for the prediction of flows in this dense regime.

The other two main approaches for modeling granular flows both track individual particles in the Lagrangian frame and resolve the collisions directly. These methods differ in their treatment of the collisions. The first method treats collisions using a hard sphere model [28, 56]. In this approximation, the collisions are assumed to be binary and instantaneous. The velocities of two particles after a collision are determined through conservation of momentum and energy. Energy losses in inelastic collisions are accounted for through a restitution coefficient and frictional effects can also be included [24]. The downside to this modelling approach is its inability to handle a particle contacting many particles at once. This situation dominates the behavior of the quasi-static and dense granular flow regimes. For this reason, hard sphere models are limited to simulations of granular flows in the rapid regime [48, 57]. The advantage of this model is its computational efficiency in comparison to the method described next. For this reason, this is the model that is used in the coupled multiphase simulations described in this paper.

The other method for resolving granular flows is known as the discrete element method (DEM) which was originally proposed by Ref. [58]. This method solves Newton's laws of motion for each individual particle. The collisional forces are modeled as a function of the overlap between particles. The advantage of this method is the ability to handle any arbitrary number of particle contacts at a given moment in time. This allows simulation of any regime of granular flow. However, the stiff nature of the equations due to the large force gradients that occur during a collision means that this method is much more expensive to solve than the hard sphere model.

There have been a wide variety of models for the forces that occur when two spheres collide. We first look at some of the normal force models that have been proposed. One of the simpler and most widely used models is the linear spring and dashpot model [59, 60]. This model is commonly used partly because of the fact that an analytical solution exists. Therefore it allows the damping in the model to be related to the restitution coefficient [61]. Another nice feature of this model is the fact that the collision duration is independent of the incoming velocity of the collision [62]. This allows one to define a time scale based on the collision duration.

Another model is based on the Hertz theory of elasticity for contact between spheres [63, 64]. This model is generally accepted to better capture the collision dynamics between spheres, however its nonlinearity causes the restitution coefficient and collision duration to be dependent on incoming velocity making it more difficult to use numerically [64].

Other models that have been used include a "locking spring" [65] and using different spring constants for the compression and rebound phases to account for inelasticity [52]. Additionally the repulsion phase of the Leonard-Jones potential, although more commonly used in molecular dynamics simulations, has also been applied to granular flow modeling [54].

There are equally as many models for the frictional forces that occur during particle collisions. The simplest model for friction is the static friction model. This model assumes the frictional force is proportional to the normal force. While not valid for every flow regime, it has proven to be relatively sucessful in the prediction of granular flows and is more computationally efficient than other models [62, 64].

The linear spring dashpot that is limited by Coulomb's law of friction is perhaps the most common friction model [52, 60]. However, this model requires calculating and storing the tangential displacement for all pairs of particles in contact and can become computationally expensive.

Another approach to modeling friction is through the use of non-spherical particles. By using particles that have concave edges, the particles are allowed to interlock and model the effects of friction without the need to introduce a separate model [54]. It has been observed that non-spherical particles do a better job capturing the granular nature of flows compared to spheres which tend to behave more fluid like [59].

Despite the variety of frictional models that can be found in literature, it has been observed that all models perform acceptably well in simulating most materials [66]. This was also observed in this work when comparing the static friction model to the linear spring dashpot model in a granular channel flow simulation.

The DEM approach to simulating granular flows is in many ways the most detailed approach to study them [54]. Numerical methods allow better access to flow properties compared to experiments where the dense, opaque nature makes them difficult to probe [67]. DEM simulations have proven to be useful in more fully understanding these flows and the development of more accurate models to predict them [64].

CHAPTER 2. PARTICLE RESOLVED DIRECT NUMERICAL SIMULATION USING THE ADAPTIVE WAVELET COLLOCATION METHOD

A paper in preparation for submission to the Journal of Computational Physics.

Ryan Goetsch and Jonathan Regele

Abstract

This work applies a new combination of techniques for the fully resolved simulation of compressible, gas-particle multiphase flows. The adaptive wavelet collocation method is used to dynamically, and efficiently, adapt the computational grid to localized flow features. An extended Brinkmann penalization technique that allows arbitrary Dirichlet, Neumann, or Robin-type immersed boundary conditions, is used to enforce the no-slip condition at particle surfaces. A hard sphere collision model is applied to resolve the particle-particle collisions. Proof of concept test cases are presented, showcasing the dynamic grid adaptation and fully resolved two-way coupling between the phases that is possible with this technique. This method shows great promise for the simulation of larger scale multiphase flows than previously practicable.

2.1 Introduction

Multiphase flows occur in a wide variety of situations that have important implications. They occur naturally in sand storms, volcanoes, and avalanches. In industrial and engineering applications, they occur in pneumatic conveyors, fluidized bed reactors, solid propellant rockets, and explosions. Research interested in understanding these complex flows has been ongoing for decades. However, due to the complexities that are inherent in these flows, they are yet to be fully understood and their prediction has been notoriously difficult [68].

Of the many types of multiphase flows, the major interest of this work is gas-particle flows. In this category, there are two major regimes characterized by the dominant physics. In the dilute phase, the physics are dominated by the fluid phase with slight modifications due to the presence of particles. The particle-particle interactions are infrequent and in many cases are neglected in simulations of flows in this regime. On the other extreme are dense flows. These flows are dominated by the particle-particle contacts. The flows on either extreme have been the focus of many studies and modeling efforts [24, 25, 9]. In many cases, industrial-scale problems of flows in these regimes can be simulated with success due to simplifying assumptions that can be made. However, flows in the intermediate regime have not been as widely studied [2].

Additionally, this work is interested in studying multiphase flows in this intermediate regime for cases where compressibility effects in the fluid phase become important. One example of such flows was studied in a recent experiment [2]. A gravity fed particle curtain with high solid volume fraction was studied inside a shock tube. The interaction between the shock wave and particle curtain was characterized through Schlieren images and pressure measurements. However, due to the high particle density, observation of the flow features inside and immediately downstream of the particle curtain was not possible, leaving many questions unanswered. Instead, this work looks to simulate these types of flows numerically in order to gain better insight on the flow features that occur.

There are many modeling techniques that have historically been applied to the simulation of multiphase flows. An overview the various methods can be found in Refs. [5, 25, 24]. Overall, these modeling techniques can be broken into two main classes, based on their treatment of the solid phase. The first main class of methods are known as two-fluid models, where both solid and gas phases are treated as continua [26]. These models require closures for the force coupling between phases in addition to the particle-particle interactions. However, general closures that are valid in the flow regime of interest have yet to be developed.

The second class of methods track individual particles in the Lagrangian frame. These methods are able to resolve the particle-particle collisions more accurately and account for the discrete nature of the particles. Within this class of methods, there are two approaches for modeling the coupling between the phases.

One approach is to solve volume averaged equations for the fluid phase [27, 28, 29, 34, 69]. The forces caused by the coupling between solid and fluid phases are computed using empirical correlations based on the fluid solution at the particle location. These correlations are most successful when the flow is relatively laminar at the particle scale. There are corrections for Reynolds number, turbulence, acceleration, and compressibility effects just to name a few [24], however there is no general and widely accepted relation that is valid over all flow regimes of interest in this work.

The other approach to modeling the coupling between phases is to directly resolve the no-slip boundary conditions at the surface of the particles. This approach allows direct calculation of the inter-phase forces while remaining valid over any flow regime without any additional modeling. The downside of this approach is the high computational cost associated with resolving the flow features near the particles.

Some interesting work has applied analytic solutions of Stokes flow in the vicinity of the particle to “transfer” the no-slip boundary condition to adjacent nodes on the fluid-phase grid [4, 36, 37]. This allows accurate integration of the fluid forces on the particle surface while avoiding the need to resolve the boundary layer of the particle. However, this technique is limited to low to moderate Reynolds number and it would be difficult to account for compressibility effects such as shock waves.

Another approach to resolving the boundary layer near the particles is through the use of body-conforming meshes [38, 70, 71]. This allows enforcing the no-slip condition directly on the nodes on the particle’s surface. However, these methods require significant numerical expense to create the mesh and quickly become impractical for moving particles.

One of the more promising techniques for resolving the boundaries of moving particles involves immersed boundary methods [39, 40]. These techniques apply forcing terms to the physical equations to enforce the no-slip conditions at the particle locations, without the need to re-compute a new mesh as the particles move. However, generally these methods require the use of a very fine and uniform computational mesh in order to resolve the boundary layer, which limits the size of problems that can be simulated.

In this work, we also make use of the immersed boundary method to resolve the no-slip condition at the particle surface. However, the prohibitive expense of using a highly resolved uniform mesh is overcome through the use of the adaptive wavelet collocation method (AWCM) [23, 72]. This technique leverages the natural ability of wavelets to compress data that is mostly smooth with localized sharp features. By keeping only the wavelets that contain important information, the computational mesh can be refined at the localized flow features, such as the boundary layers and shock waves, while allowing a coarser grid in smoother regions of the solutions. Best of all, this mesh refinement occurs dynamically and with little additional computational expense required. The AWCM, applied to the fully resolved simulation of gas-particle flows, allows these simulations to be performed using much fewer computational resources. This opens up the possibility of simulating much larger multiphase systems than previously practical.

The remainder of this paper will be organized as follows. First, the governing equations and numerical techniques for the fluid phase will be discussed in Section 2.2. Next, the solution of the solid phase is discussed in Section 2.3, followed by a discussion of the coupling between phases in Section 2.4. The results will be presented in Section 2.5, and a summary and conclusions in Section 2.6.

2.2 Fluid phase

In this section, a discussion of the governing equations and numerical techniques used to solve the fluid phase will be discussed in isolation from the solid phase.

2.2.1 Governing equations

The evolution of the fluid phase is governed by the Navier-Stokes equations. This work follows the non-dimensional formulation given in Ref. [21]

$$\frac{\partial \rho}{\partial t} = -\frac{\partial \rho u_j}{\partial x_j} \tag{2.1}$$

$$\frac{\partial \rho u_j}{\partial t} = -\frac{\partial(\rho u_i u_j)}{\partial x_j} - \frac{\partial p}{\partial x_i} + \frac{1}{Re_a}\frac{\partial \tau_{ij}}{\partial x_j} \tag{2.2}$$

$$\frac{\partial \rho e}{\partial t} = -\frac{\partial}{\partial x_j}\left[(\rho e + p)u_j\right] + \frac{1}{Re_a}\frac{\partial(u_i\tau_{ij})}{\partial x_j} + \frac{1}{\gamma - 1}\frac{1}{Re_a Pr}\frac{\partial}{\partial x_j}\left(\mu\frac{\partial T}{\partial x_j}\right), \tag{2.3}$$

where the non-dimensional equation of state is

$$p = \frac{\rho T}{\gamma}, \tag{2.4}$$

and

$$\tau_{ij} = \mu\left(\frac{\partial u_i}{\partial x_j} + \frac{\partial u_j}{\partial x_i} - \frac{2}{3}\frac{\partial u_k}{\partial x_k}\delta_{ij}\right) \tag{2.5}$$

$$e = \frac{1}{2}u_i u_i + \frac{c_p T}{\gamma - 1} - \frac{p}{\rho}. \tag{2.6}$$

In the above equations, the velocity is non-dimensionalized by the reference speed of sound c_0, time by L/c_0, specific energy by c_0^2, density by ρ_0, pressure by $\rho_0 c_0^2$, viscosity by μ_0, thermal conductivity by $\mu_0 c_{p_0}$, and temperature by T_0, where all quantities with subscript "0" denote the reference state and L is the reference length scale. The temperature dependence of μ is assumed to follow Sutherland's law [73]

$$\mu = \frac{1 + S_1}{T + S_1}T^{3/2} \tag{2.7}$$

where S_1 is normalized by T_0.

2.2.2 Numerical methods

In order to fully resolve the flow features that are present around the solid particles, high resolution is needed. However, far from the particles the resolution requirements are not as demanding. This type of problem lends itself readily to the use of an adaptive grid. In this work, an adaptive wavelet collocation method (AWCM) is used. A brief overview is provided here, while more details can be found in Refs. [74, 75, 72, 23, 76]. In this method, each grid point is associated with a wavelet. A function u in multiple dimensions is decomposed as

$$u(\boldsymbol{x}) = \sum_{k\in\mathcal{K}^0} c^0_{\boldsymbol{k}}\phi^0_{\boldsymbol{k}}(\boldsymbol{x}) + \sum_{j=0}^{\infty}\sum_{\mu=1}^{2^n-1}\sum_{l\in\mathcal{L}^{\mu,j}} d^{\mu,j}_{\boldsymbol{l}}\psi^{\mu,j}_{\boldsymbol{l}}(\boldsymbol{x}), \tag{2.8}$$

where ϕ is a scaling function with coefficient c and ψ is a wavelet with coefficient d. The superscript j indicates the level of resolution, the subscripts k and l indicate the spatial index, and μ is the wavelet family. The sets of integers $\mathcal{K}^0$ and $\mathcal{L}^{\mu,j}$ are all integers associated with the scaling functions at the zeroth level of resolution, and the wavelets at the j^{th} level of resolution and family μ, respectively.

A thresholding parameter ϵ is used to determine the wavelets that are important for representing the solution. It has been shown that the error in the solution is bounded and is controlled by ϵ [77]. This allows a solution with a known level of accuracy on much fewer grid points than traditionally necessary.

In this work, the Crank-Nicholson method is used for time integration and a fourth order accurate spatial discretization is used. However, any method can be used, as this work is not dependent on the time integration or spatial discretization methods.

2.3 Solid phase

The solid phase is represented as cylindrical or spherical (2-D and 3-D, respectively) particles. The free flight motion, collision dynamics, and time integration are discussed in this section.

2.3.1 Free flight motion

The motion of a particle in the absence of any collisions is governed by Newtons second law for linear and angular motion

$$m\frac{d^2\boldsymbol{x}}{dt^2} = \boldsymbol{F} \tag{2.9}$$

$$I\frac{d\boldsymbol{\omega}}{dt} = \boldsymbol{T}, \tag{2.10}$$

where m, $\boldsymbol{x}$, $\boldsymbol{F}$, I, $\boldsymbol{\omega}$, and $\boldsymbol{T}$ are the mass, position vector, net external force vector, moment of inertia, angular velocity vector, and net external torque vector, respectively. Note that for spheres/cylinders, the angular position is not important, therefore it is not solved for. For the case where $\boldsymbol{F}$ and $\boldsymbol{T}$ are constant, the following equations are obtained

$$\boldsymbol{x}(t) = \boldsymbol{x}(0) + \boldsymbol{v}(0)t + \frac{1}{2}\frac{\boldsymbol{F}}{m}t^2 \tag{2.11}$$

$$\boldsymbol{v}(t) = \boldsymbol{v}(0) + \frac{\boldsymbol{F}}{m}t \tag{2.12}$$

$$\boldsymbol{\omega}(t) = \boldsymbol{\omega}(0) + \frac{\boldsymbol{T}}{I}t, \tag{2.13}$$

where $\boldsymbol{v}$ is the particle velocity vector.

2.3.2 Collision model

In this work, the hard sphere approximation is used to model the collisions between spherical particles. Collisions are assumed to be instantaneous and binary and the particle deformation is neglected. The initial velocities $\boldsymbol{v}^{(0)}$ and angular velocities $\boldsymbol{\omega}^{(0)}$ are known prior to the instant of the collision. The post collision conditions are computed as a function of the impulsive force exerted between the particles using the conservation of linear and angular momentum. The details of the formulation can be found in Ref. [24]. The result is a relation between the pre-collision and post collision velocities for each particle.

First, we define some quantities. The relative velocity of the particle centers $\boldsymbol{G}^{(0)}$ and points of contact $\boldsymbol{G}_c^{(0)}$ at the instant before contact are

$$\boldsymbol{G}^{(0)} = \boldsymbol{v}_1^{(0)} - \boldsymbol{v}_2^{(0)} \tag{2.14}$$

$$\boldsymbol{G}_c^{(0)} = \boldsymbol{G}^{(0)} + r_1\boldsymbol{\omega}_1^{(0)} \times \boldsymbol{n} + r_2\boldsymbol{\omega}_2^{(0)} \times \boldsymbol{n}, \tag{2.15}$$

respectively. The tangential component of $\boldsymbol{G}_c^{(0)}$ is

$$\boldsymbol{G}_{ct}^{(0)} = \boldsymbol{G}_c^{(0)} - \left(\boldsymbol{G}_c^{(0)} \cdot \boldsymbol{n}\right)\boldsymbol{n}. \tag{2.16}$$

In addition, the quantities μ and e, the friction and restitution coefficients respectively, are taken to be known material properties. These parameters control the energy losses that occur during the collision.

There are two possible situations that need to be considered when two particles collide. The first occurs when the particles slide for the entire duration of the collision. This condition happens when the inequality

$$\frac{\boldsymbol{n}\cdot\boldsymbol{G}^{(0)}}{\left|\boldsymbol{G}_{ct}^{(0)}\right|} < -\frac{2}{7}\frac{m_1 m_2}{m_1+m_2}\left|\boldsymbol{G}_{ct}^{(0)}\right| \tag{2.17}$$

is satisfied. In that case, the post-collision velocities are

$$\boldsymbol{v}_1 = \boldsymbol{v}_1^{(0)} - (\boldsymbol{n}+\mu\boldsymbol{t})\left(\boldsymbol{n}\cdot\boldsymbol{G}^{(0)}\right)(1+e)\frac{m_2}{m_1+m_2} \tag{2.18}$$

$$\boldsymbol{v}_2 = \boldsymbol{v}_2^{(0)} + (\boldsymbol{n}+\mu\boldsymbol{t})\left(\boldsymbol{n}\cdot\boldsymbol{G}^{(0)}\right)(1+e)\frac{m_1}{m_1+m_2} \tag{2.19}$$

$$\boldsymbol{\omega}_1 = \boldsymbol{\omega}_1^{(0)} - \left(\frac{5}{2r_1}\right)\left(\boldsymbol{n}\cdot\boldsymbol{G}^{(0)}\right)(\boldsymbol{n}\times\boldsymbol{t})\mu(1+e)\frac{m_2}{m_1+m_2} \tag{2.20}$$

$$\boldsymbol{\omega}_2 = \boldsymbol{\omega}_2^{(0)} - \left(\frac{5}{2r_2}\right)\left(\boldsymbol{n}\cdot\boldsymbol{G}^{(0)}\right)(\boldsymbol{n}\times\boldsymbol{t})\mu(1+e)\frac{m_1}{m_1+m_2}. \tag{2.21}$$

The case where Eq. 2.17 is not satisfied indicates that the particles' relative sliding at the contact point goes to zero at some point during the collision. The post collision velocities for this case become

$$\boldsymbol{v}_1 = \boldsymbol{v}_1^{(0)} - \left\{(1+e)\left(\boldsymbol{n}\cdot\boldsymbol{G}^{(0)}\right)\boldsymbol{n} + \frac{2}{7}\left|\boldsymbol{G}_{ct}^{(0)}\right|\boldsymbol{t}\right\}\frac{m_2}{m_1+m_2} \tag{2.22}$$

$$\boldsymbol{v}_2 = \boldsymbol{v}_2^{(0)} + \left\{(1+e)\left(\boldsymbol{n}\cdot\boldsymbol{G}^{(0)}\right)\boldsymbol{n} + \frac{2}{7}\left|\boldsymbol{G}_{ct}^{(0)}\right|\boldsymbol{t}\right\}\frac{m_1}{m_1+m_2} \tag{2.23}$$

$$\boldsymbol{\omega}_1 = \boldsymbol{\omega}_1^{(0)} - \frac{5}{7r_1}\left|\boldsymbol{G}_{ct}^{(0)}\right|(\boldsymbol{n}\times\boldsymbol{t})\frac{m_2}{m_1+m_2} \tag{2.24}$$

$$\boldsymbol{\omega}_2 = \boldsymbol{\omega}_2^{(0)} - \frac{5}{7r_2}\left|\boldsymbol{G}_{ct}^{(0)}\right|(\boldsymbol{n}\times\boldsymbol{t})\frac{m_1}{m_1+m_2} \tag{2.25}$$

2.3.3 Collision time and time advancement

Two particles will first come into contact when the following equation is satisfied

$$|\boldsymbol{x}_i(t) - \boldsymbol{x}_j(t)| = r_i + r_j, \tag{2.26}$$

where the indices i and j represent two different particles. Using Eq. 2.11 for $\boldsymbol{x}(t)$, this equation becomes a fourth order polynomial in time.

In the special case that the acceleration is the same for all particles, the equation is reduced to a second order polynomial in time allowing an algebraic solution. This situation arises when only gravitational forces are acting on the particles, for example. In these cases, efficient algorithms known as event-driven algorithms can be used [78, 56]. The collision time for all pairs of particles can be computed with little numerical expense, allowing the system to be advanced on a collision by collision basis. This allows very large time steps to be taken and the system to be advanced through time in an efficient manner.

However, in this work the fluid forces result in non-equal accelerations. Therefore, a numerical solution to the full fourth order polynomial is required. Because this is much more computationally expensive than an algebraic solution, an event-driven approach is not practical.

For this reason, we use the approach described in Sect. 4.3 of Ref. [78] where collisions are detected retrospectively. The simulation is advanced through time at a regular interval (in this case, the same Δt as required for the fluid phase) using the free flight equations 2.11–2.13. After each step, collisions are detected by checking for overlaps between pairs of particles. When an overlap is detected, the time that the collision should have occurred is bracketed by the starting and ending times of the time step and a numerical algorithm can be used to solve for the actual time of the collision.

In this work, the hybrid Newton-Raphson/bisection method described in Ref. [79] is used to solve for the collision time. This method combines the fast convergence of the Newton-Raphson method with the robustness of the bisection method.

There are situations where complex sequences of collisions occur for a given particle during a time step. These situations require special care to properly resolve. The approach used here involves subdividing time step size until the sequence of collisions can be solved using the simple algorithm described above. Further details about the algorithm and can be found in Ref. [78].

2.4 Fluid-solid coupling

The equations and numerical techniques for both the fluid and solid phases have been discussed above. In this section, the techniques for coupling the two phases are discussed.

2.4.1 Immersed boundary method

The desired boundary conditions for a solid particle in a viscous fluid are a no-slip condition for the velocity and adiabatic or heat flux condition on temperature. One method of enforcing these conditions is through a body-fitted mesh, allowing the above constraints to be enforced directly on the surface of the particle. However, computing a body fitted mesh at every time step for moving objects is very computationally expensive. The alternative, used in this work, is to use immersed boundary conditions.

Immersed boundary conditions work by adding forcing terms to the governing equations that enforce the desired boundary conditions without the need for a body-conforming mesh. This work uses an extended Brinkman penalization approach described in Ref. [21]. This approach allows any Dirichlet, Neumann, or Robin type boundary condition to be specified on a general hyperbolic or parabolic system of evolutionary equations. Additionally, the boundary conditions can be easily applied to both integrated and non-integrated variables.

As discussed in Ref. [21], the governing equations 2.1–2.3 are penalized as follows

$$\begin{aligned}
\frac{\partial \rho}{\partial t} =& (1-\chi)\times \mathrm{RHS} - \frac{\chi}{\eta_c}\left[\eta_k \frac{\partial \rho}{\partial x_k} - \phi\right] && (2.27)\\
\frac{\partial \rho u_i}{\partial t} =& (1-\chi)\times \mathrm{RHS} && (2.28)\\
& -\chi\left[\frac{1}{\eta_b}\rho(u_i-u_{0i}) - \rho\nu_n \frac{\partial^2 u_i}{\partial x_j \partial x_j} + \frac{1}{\eta_c} u_i \left(n_k \frac{\partial \rho}{\partial x_k} - \phi\right)\right] &&\\
\frac{\partial \rho e}{\partial t} =& (1-\chi)\times \mathrm{RHS} - \chi\left[\frac{1}{\eta_c}\left(\eta_k \frac{\partial \rho e}{\partial x_k}\right) \frac{\rho(u_j-u_{0j})u_j}{\eta_b} - \frac{\rho u_j}{\eta_c}\eta_k \frac{\partial u_j}{\partial x_k}\right. && (2.29)\\
& \left. -\rho u_j \nu_n \frac{\partial^2 u_j}{\partial x_i \partial x_i} - \frac{1}{\eta_c} e\phi - \frac{1}{\eta_c} c_v \rho q\right], &&
\end{aligned}$$

where χ is a mask function that is unity inside the object and zero outside, RHS indicates the right hand side of Eqns. 2.1–2.3, and n_k is the inward facing surface normal of the object. The velocity u_{0i} is the velocity of the object. The parameters η_c, η_k, and ν_n control the accuracy and numerical stability as described in Ref. [21]. Note that outside the object, the equations become the same as the Navier Stokes equations, and inside are governed by only the penalization terms. In the penealization for ρ, the quantity ϕ is governed by the equation

$$\frac{\partial \phi}{\partial t} = -\frac{\chi}{\eta_c} n_k \frac{\partial \phi}{\partial x_k}. \qquad (2.30)$$

The quantity ϕ allows a Neumann condition on ρ that is passively controlled by the fluid physics. The error from these penalized boundary conditions converges as $O(\eta_c, \eta_b^{1/2})$.

2.4.2 Force calculation

The force from a viscous fluid acting on a differential surface dS with unit normal n_j is

$$f_i = \sigma_{ij} n_j, \tag{2.31}$$

where $\sigma_{ij} = -p\delta_{ij} + \tau_{ij}$. The total force acting on a particle is the integral over the surface

$$F_i = \iint_{\delta O_m} \sigma_{ij} n_j dS = \iiint_{O_m} \frac{\partial \sigma_{ij}}{\partial x_j} dV \approx \sum_{k \in O_m} \left(\frac{\partial \sigma_{ij}}{\partial x_j} \right)_k \Delta V_k, \tag{2.32}$$

where the divergence theorem is used to change from a surface integral to a volume integral and a summation over all k grid cells in O_m is used to approximate the integral on a discrete grid. O_m represents the region inside the particle and δO_m is the outer surface.

The net torque can be computed using a similar formulation, however this formulation is restricted to spherical particles in 3-D or cylinders in 2-D. Using this restriction, the torque acting on dS is related to f_i by

$$t_i = r\epsilon_{jki} n_j f_k \tag{2.33}$$

where ϵ is the permutation symbol used to represent the vector cross product in index notation and r is the particle radius. This is then integrated over δO_m to obtain the net torque, noting that r is a constant for spherical particles

$$\begin{aligned} T_i =& r \iint_{\delta O_m} \epsilon_{jki} n_j (\sigma_{km} n_m) dS = r \iiint_{O_m} \epsilon_{jki} \frac{\partial \sigma_{km} n_m}{\partial x_j} dV \\ \approx& \sum_{l \in O_m} \left(\epsilon_{jki} \frac{\partial \sigma_{km} n_m}{\partial x_j} \right)_l \Delta V_l, \end{aligned} \tag{2.34}$$

where a generalized Stokes theorem is used to change from a surface integral to a volume integral.

Note that the use of the divergence and Stokes theorems here is justified because the penalized solution inside the particles is continuous. Even though this solution is not physical, its continuity allows us to evaluate the forces at the surface by a volume integral over the interior.

2.4.3 Time advancement

The current method of coupling the time integrations of the solid and fluid phases takes a leap-frog approach. The first step is computing the fluid forces $\boldsymbol{F}^n$ and $\boldsymbol{T}^n$ acting on the particles in Eqns. 2.32 and 2.34 using the current fluid solution, where n indicates the current iteration. The particle locations and velocities are updated using the equations in Section 2.3.2, with the assumption that $\boldsymbol{F}^n$ and $\boldsymbol{T}^n$ are constant through Δt, yielding $\boldsymbol{x}^{n+1}$, $\boldsymbol{v}^{n+1}$, and $\boldsymbol{\omega}^{n+1}$. Next, the immersed boundary conditions, enforced through the penalized Navier-Stokes equations 2.27–2.29, are updated using these updated particle positions and velocities. The fluid phase is then advanced to t^{n+1} with the assumption that the particle positions and velocities do not change during the time step. This completes the time step and the process is repeated until the desired ending time is reached. In future work, a higher order method will be used to couple the time steps of the solid and fluid phases.

2.5 Results

This section presents some results as a proof of concept for our multiphase flow simulation technique. Qualitative validation will be the subject of future work. However, validity of the immersed boundary method has been throughly investigated in Ref. [21]. The accuracy of the flow solution for both stationary and moving cylinders was validated against previous numerical works and experiments. Quantities such as the boundary layer separation point, and lift and drag forces showed good agreement with previous results.

In addition, the hard sphere collision has also been verified independent of the fluid phase. Simulations were performed and validated by verifying that total system energy and momentum are conserved through collisions. These results can be found in Appendix A.

Figure 2.1 shows how the AWCM is able to adapt the grid to the surfaces of the particles. In these test cases, there is no fluid solution to adapt to, therefore the grid is only adapting to χ. These cases show how the AWCM allows fully resolved computation of the particles' boundary layers while allowing a coarse grid in regions where the resolution is not needed,

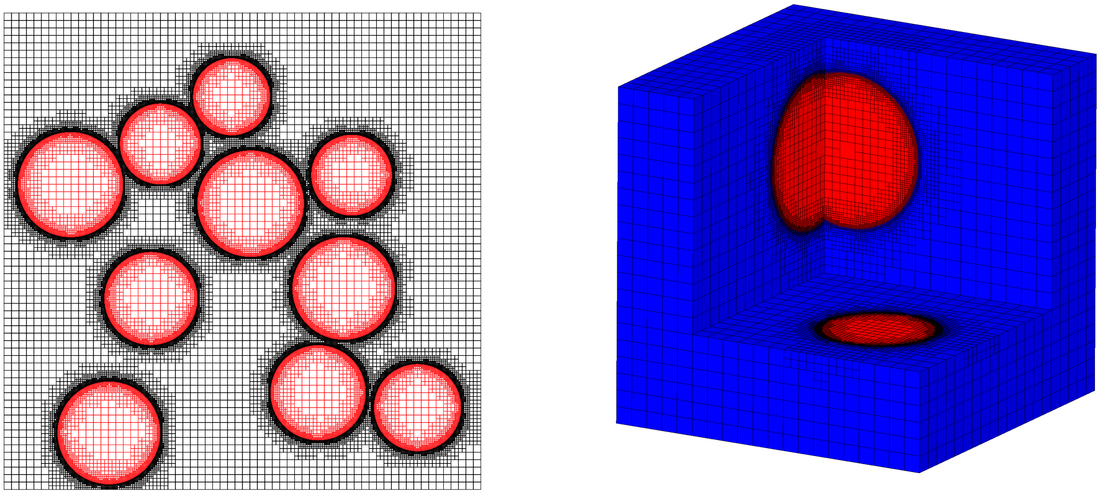

Figure 2.1 Snapshot in time of the computational grid dynamically adapting to χ for moving particles in 2-D (left) and 3-D (right). The red regions are inside the particles where $\chi = 1$, and $\chi = 0$ elsewhere.

including inside the particles. In cases where the fluid is also present, the grid will also adapt to flow features such as shock waves.

This method was also tested in 2-D and 3-D when the fluid is present. The results for a 2-D simulation are shown in Fig. 2.2. In this case, two cylindrical particles start on the upper right and lower left corners of the domain and move toward the center. A collision occurs in the center of the domain after which they move away from each other toward the opposite corners of the domain. The acoustic Reynolds number is 1,000, the particles' non-dimensional speed is 0.3, and there are 64 points per particle diameter at the maximum level of resolution. During the simulation, only 0.3 % of the possible grid points are needed, highlighting the computational savings possible when using an adaptive grid. The results are colored by the out-of-plane component of vorticity to highlight the unsteady vortex shedding occurring before and after the particle collision.

2.6 Summary and conclusions

The goal of this work is the fully resolved simulation of compressible gas-particle multiphase flows. Typically, fully resolved approaches are limited by the computational expense due to

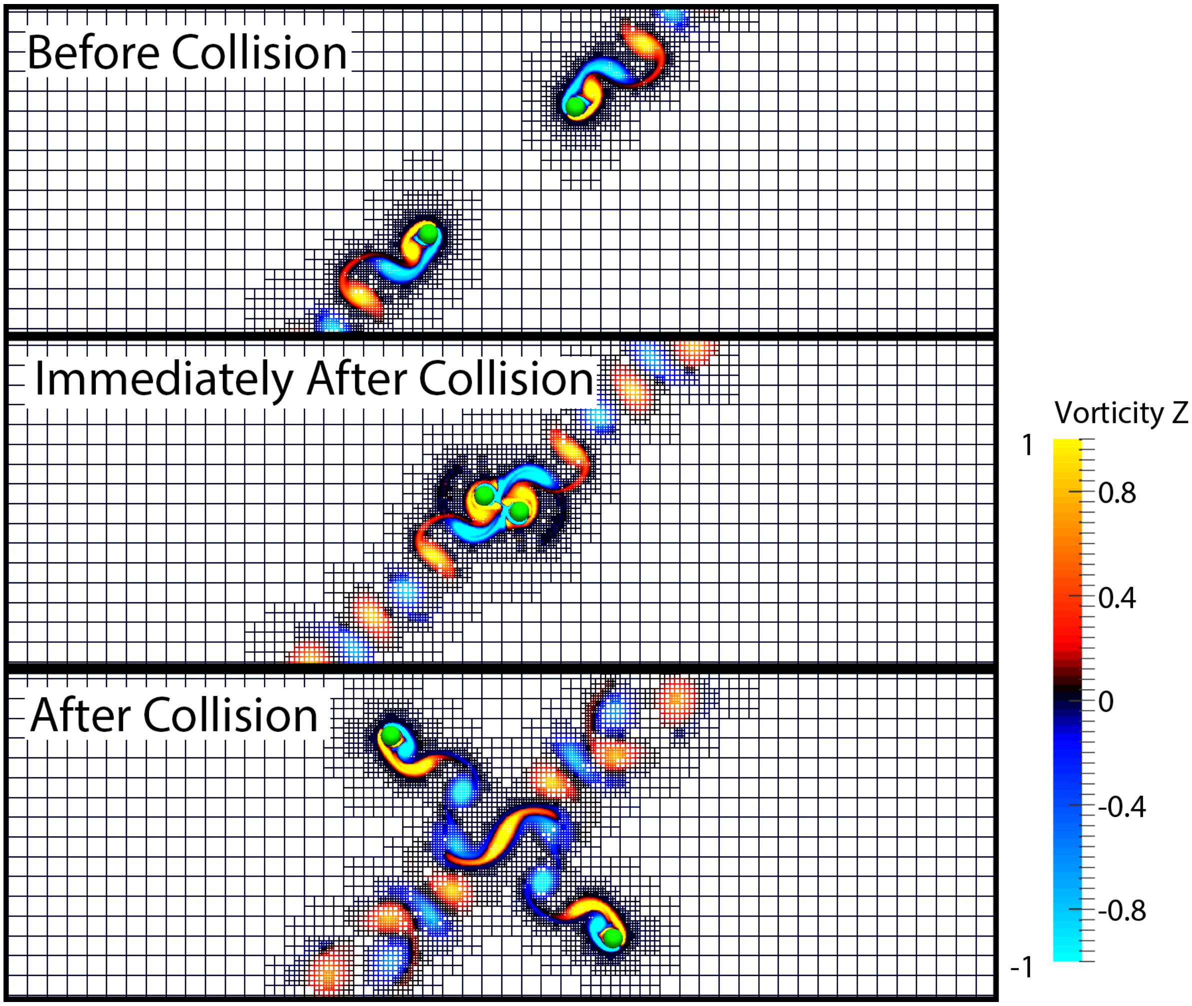

Figure 2.2 Example result for a 2-D simulation with two particles before and after undergoing a collision. The grid lines are colored by the vorticity.

grid generation or high cost of a uniform, high resolution grid. In this work, the AWCM is used in conjunction with an extended Brinkmann penalization immersed boundary technique. The use of the AWCM allows the computational grid to be refined only in the necessary regions without the typical overhead of adaptive mesh techniques. A hard sphere collision model is implemented to handle particle-particle collisions.

The wavelet-based grid adaptation is first tested with moving particles in 2-D and 3-D in isolation from the fluid phase. The grid is seen to dynamically adapt to the edges of the particles, which will allow full resolution of the particle boundary layers.

Additionally, tests were conducted that show the two-way coupling possible between the solid and fluid phases. In 2-D, results are shown that exhibit a particle-particle collision and unsteady vortex shedding from two cylinders, showcasing the possibilities of this approach.

In future work, we look to apply this method to the simulation of laboratory-scale problems such as the multiphase shock tube tested in Ref. [2]. This method shows great promise in simulating large scale problems, allowing a detailed look into the flow features that occur in this complex regime of fluid flow.

CHAPTER 3. DEM PREDICTION OF PARTICLE CURTAIN PROPERTIES

A paper submitted to Physical Review E.

Ryan Goetsch and Jonathan Regele

Abstract

The discrete element method (DEM) is used to predict the properties of a particle curtain created by the three-dimensional granular flow through a hopper constricted by a slit opening. The profiles of the mean and fluctuation velocity components and solid volume fraction within the particle curtain are estimated. The model is validated against experimental measurements of the mean and fluctuation velocity profiles in a granular channel flow. Good agreement is observed between the experimental channel flow measurements and our DEM simulations. The approach is extended to model the behavior of the particle curtain after it exits the hopper. The model predictions suggest that the volume fraction is not uniform across the curtain as expected from experimental results.

3.1 Introduction

Multiphase flows occur in a wide variety of phenomenon. Some, such as fluidized bed reactors, have very important industrial applications. For this reason, these types of flows have been actively studied for decades. There has been success in modeling these flows when the solid phase is in either the dilute or densely packed regimes. However, the modeling of compressible flows when the solid phase has a volume fraction between these extremes has lagged behind [2]. Additionally, this intermediate regime of multiphase flows has seen relatively little experimental investigation due to the difficulties in isolating and measuring the high solid volume fraction regions.

A recent experiment has been developed that investigates the interaction between a shock wave and a high volume fraction particle curtain [2]. Schlieren images in conjunction with pressure measurements are used to characterize the flow features. However, due to the high volume fraction of particles within the particle curtain, the flow features are not directly observable. For this reason, there is interest in simulating the shock wave-particle cloud interaction numerically, in order to observe the flow features at a greater level of detail. However, a numerical simulation requires accurate initial conditions, including detailed information about the particle curtain. Some important quantities include the profile of the volume fraction as well as the mean and fluctuation velocity components of the particles in the curtain. The particle curtain used in this experiment was generated by the granular flow of glass beads through a hopper with a slit opening. Detailed information about the particle curtain is not available experimentally, therefore it must be predicted through alternate methods.

The flow of granular materials have been notoriously difficult to model and predict. This is partly due to the wide range of behaviors that granular flows can exhibit. They are known to exhibit the behavior of a solid, liquid or gas depending on the amount of external energy supplied to the system [41, 42]. Additionally, accurate experimental measurements of opaque granular materials have many difficulties, which in part has lead to a significant lack of experimental information [64, 67, 80]. This wide range of behaviors and lack of information has complicated the efforts in obtaining a universal continuum model [64, 81]. For these reasons, much of the research in this field has relied on numerical simulations using a Lagrangian approach, where the trajectories of individual grains within a granular media are obtained. In many ways these numerical simulations have lead experimental work in obtaining the detailed measurements needed for the development of models [54, 64].

Perhaps the most widely used method used in these numerical studies is the discrete element method (DEM), which was originally formulated by Cundall and Strack [58]. In this method, the motion of individual grains is obtained through numerical integration of Newton's second law. The grains are allowed to slightly overlap, and the collisional forces are modeled as a function of the overlap distance. In this work, a solver using the discrete element method is used to predict the properties of the particle curtain.

The primary objective of this work is to use DEM simulations to better characterize the particle flow conditions exiting the hopper found in Ref. [2]. In order to have confidence in the results from the numerical simulation, we first look to validate the model with detailed experimental measurements. While there is little to no experimental work studying the properties of a particle curtain similar to that used in Ref [2], there are a few classes of basic granular flows that have been thoroughly studied. These include plane shear, annular shear, vertical channel flows, inclined plane, heap flow, and rotating drums [43]. The flow that is most similar to the particle curtain of interest is the vertical channel flow, as this flow exists in the feed hopper region. In an experiment by Natarajan, *et al.* [3], the profiles of the mean and fluctuation velocities within a channel were measured through optical particle tracking. These results are used as a benchmark to show that the model is able to predict the properties of the particle curtain below the channel.

The paper is organized as follows. First, the numerical approach will be discussed in Section 3.2 followed by a validation of the model in Section 3.3. The prediction of the particle curtain properties will then be discussed in Section 3.4. Finally, a summary and final conclusions will be included in Section 3.5.

3.2 Numerical model

3.2.1 Equations of motion

The motion of each individual grain in a granular medium is fully described by Newton's second law for linear and angular motion

$$m_i \frac{d^2 \boldsymbol{r}_i}{dt^2} = \boldsymbol{F_i} \tag{3.1}$$

$$I_i \frac{d\boldsymbol{\omega}_i}{dt} = \boldsymbol{T}_i, \tag{3.2}$$

where the subscript i represents the particle index, m is the mass, $\boldsymbol{r}$ is the position vector, t is time, $\boldsymbol{F}$ is the total external force, I is the moment of inertia, $\boldsymbol{\omega}$ is the angular velocity vector, and $\boldsymbol{T}$ is the total external torque acting on the particle.

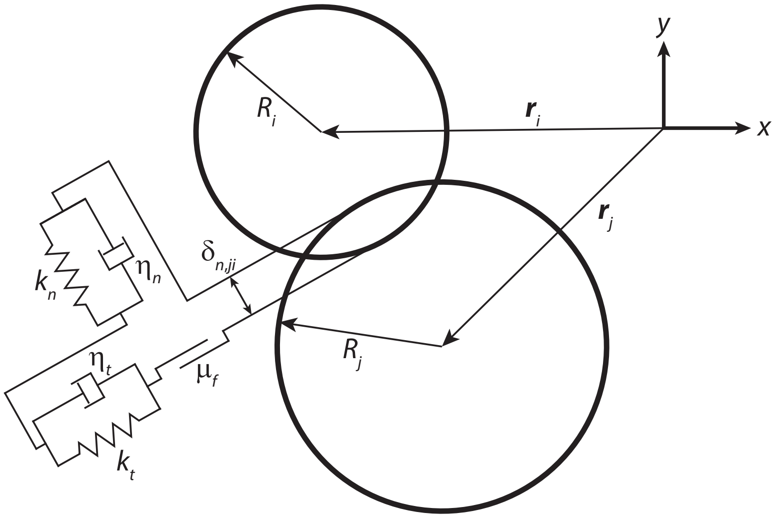

Figure 3.1 Diagram of the linear spring and dashpot model for the contact forces in the normal and tangential directions for two overlapping spheres as described in the text.

The external force $\boldsymbol{F}_i$ is commonly broken into components that are each modeled separately

$$\boldsymbol{F}_i = \sum_{j,\ j\neq i} (\boldsymbol{F}_{n,ji} + \boldsymbol{F}_{t,ji}) + \boldsymbol{F}_{ext,i}, \tag{3.3}$$

where $\boldsymbol{F}_{n,ji}$ and $\boldsymbol{F}_{t,ji}$ are the normal and tangential components, respectively, of the contact force acting on particle i due to particle j. The term $\boldsymbol{F}_{ext,i}$ represents any additional external forces not caused by particle-particle contact including gravitational forces, contact with walls, and fluid forces. The torque on the particle i is related to the force acting on it through

$$\boldsymbol{T}_i = \sum_{j,\ j\neq i} (R_i \boldsymbol{n}_{ji} \times \boldsymbol{F}_{t,ji}), \tag{3.4}$$

where $\boldsymbol{n}_{ji}$ is the normal unit vector that points from the center of particle i to the center of particle j and R_i is the radius of particle i.

3.2.2 Collision model

The first part of this section focuses on the normal component, $\boldsymbol{F}_{n,ji}$, of the contact force between two spheres. One of the most simple and widely used models is a linear-spring and dashpot as depicted in Fig. 3.1. In this model, the normal contact force is given by

$$\boldsymbol{F}_{n,ji} = -k_n \delta_{n,ji} \boldsymbol{n}_{ji} - \eta_n \boldsymbol{v}_{n,ji} \tag{3.5}$$

where k_n is the normal spring stiffness, and $\boldsymbol{v}_{n,ji}$ is the normal component of the velocity of particle j relative to particle i. The normal component of the overlap $\delta_{n,ji}$, unit normal vector, and velocity of the surface of particle j relative to i at the point of contact are

$$\delta_{n,ji} = (R_i + R_j) - |\boldsymbol{r}_j - \boldsymbol{r}_i| \tag{3.6}$$

$$\boldsymbol{n}_{ji} = \frac{\boldsymbol{r}_j - \boldsymbol{r}_i}{|\boldsymbol{r}_j - \boldsymbol{r}_i|} \tag{3.7}$$

$$\boldsymbol{v}_{ji} = (\boldsymbol{v}_j - \boldsymbol{v}_i) + (R_i\boldsymbol{\omega}_i + R_j\boldsymbol{\omega}_j) \times \boldsymbol{n}_{ji}, \tag{3.8}$$

respectively, where the normal component of the relative velocity is

$$\boldsymbol{v}_{n,ji} = (\boldsymbol{v}_{ji} \cdot \boldsymbol{n}_{ji})\boldsymbol{n}_{ji}. \tag{3.9}$$

The damping coefficient η_n is related to the restitution coefficient e [82, 83, 61]

$$\eta_n = \frac{-2\ln e\sqrt{m^* k_n}}{\sqrt{\pi^2 + \ln^2 e}} \quad (e \neq 0) \tag{3.10}$$

where it can take values in the range $0 < e \leq 1$ and m^* is

$$m^* = \left(\frac{1}{m_i} + \frac{1}{m_j}\right)^{-1}. \tag{3.11}$$

We now look at the tangential component of the contact force $\boldsymbol{F}_{t,ji}$. An analogous linear-spring and damper model is commonly used. However, in the tangential direction this force is limited by a Coulomb-type sliding friction force

$$\boldsymbol{F}_{t,ji} = \begin{cases} -k_t\boldsymbol{\delta}_t - \eta_t\boldsymbol{v}_{t,ji}, & |\boldsymbol{F}_{t,ji}| \leq \mu|\boldsymbol{F}_{n,ji}| \\ -\mu_f|\boldsymbol{F}_{n,ji}|\boldsymbol{t}_{ji}, & |\boldsymbol{F}_{t,ji}| > \mu|\boldsymbol{F}_{n,ji}|, \end{cases} \tag{3.12}$$

where k_t, $\boldsymbol{\delta}_t$, η_t, and μ are the tangential stiffness, relative displacement, damping coefficient, and coefficient of friction, respectively. The tangential relative velocity and unit vector are found using

$$\boldsymbol{v}_{t,ji} = \boldsymbol{v}_{ji} - \boldsymbol{v}_{n,ji} \tag{3.13}$$

$$\boldsymbol{t}_{ji} = \frac{\boldsymbol{v}_{t,ji}}{|\boldsymbol{v}_{t,ji}|}. \tag{3.14}$$

The tangential relative displacement in 2-D is calculated by integrating the tangential velocity

$$\boldsymbol{\delta}_t = \boldsymbol{\delta}_{t_0} + \int_{t_0}^{t} \boldsymbol{v}_{t,ji}(t')\,dt'. \tag{3.15}$$

However, this formula requires storing δ for all pairs of particles that are in contact and adds significant computational expense. Additionally, in 3-D simulations, the rotation of the contact plane requires coordinate transformations between time steps [83].

An alternative friction model that eliminates the need to calculate Eq. 3.15 is the static friction model. The friction force is represented as simply the static friction component of the equation above

$$\boldsymbol{F}_{t,ji} = -\mu_f |\boldsymbol{F}_{n,ji}| \boldsymbol{t}_{ji}. \tag{3.16}$$

As discussed in Ref. [62], this simplified model is a good compromise between accuracy and computational cost for granular flows dominated by sustained contact. This is further investigated in Appendix B.

The same equations used to compute contact forces between particles are also used to compute the particle-wall contact forces. These contact forces occur at non-periodic system boundaries and the plane segments that constrict the channel to a slit opening at the bottom. In these collisions, the closest point to the center of the particle that lies on the wall is treated as particle j with $R_j = 0$ and $m_j = \infty$. In effect, this treats a wall as a point particle with infinite mass. This allows the calculation of $\boldsymbol{F}_n$ and $\boldsymbol{F}_t$ using the same models as for particle-particle collisions.

3.2.3 Time integration

The equations of motion of the system of particles described in Section 3.2.1 above are a coupled system of ordinary differential equations. The initial conditions of the particles are known, therefore this represents an initial value problem where the solution can be marched through time. In this work, a second order Runge-Kutta method is used.

Because of the stiff nature of the equations of motion, a very small time step is needed to properly resolve the collisions and ensure conservation of energy. It is common practice to restrict the time step by forcing N steps to occur within the duration of a collision. The exact solution to the equations of motion shows that the collision duration is [62]

$$\tau = \sqrt{[\pi^2 + \ln(e)^2]\frac{m^*}{k_n}}. \tag{3.17}$$

The maximum allowable time step is then $dt_{\max} = \tau/N$. When simulating a system of non uniform diameter particles, the smallest value of $dt_{\max}$ for all pairs of particles is chosen to ensure at least N time steps are taken during each collision. In previous work, N values of 10–100 have been used [64, 62, 59]. In this work, the time step size is chosen such that $N \geq 50$ is enforced unless otherwise specified.

3.2.4 Initial conditions

In all of the simulations in this work, the desired initial condition is a fully packed and static bed of particles in a closed hopper. This allows the hopper to be opened at the start of the simulation and the particles then flow out of the hopper. However, generating a densely packed bed of particles directly is not a trivial problem. Instead, the particles are first initialized in a non-packed arrangement such as randomly placed in the domain or placed on a uniform lattice. Then, with a wall placed at the bottom of the hopper to close it, the particles are allowed to fall under the influence of gravity and settle to form the desired densely packed configuration. This process can be sped up by using larger than physical values for e and μ in order to quickly damp out the kinetic energy from the system [56].

3.2.5 Periodic recycling of particles

This work is focused on studying the properties of steady state granular flows, where the statistics are stationary in time. This can be accomplished numerically by the use of periodic boundary conditions, allowing particles leaving the bottom of the domain to re-enter through the top. There has been numerical work where this has been done without any special treatment [59]. However, in the present work, spurious fluctuations were observed caused by the re-entering particles impacting the top of the particle bed. Other work has used a technique were particles leaving were placed at the lowest location on the top of the particle bed with zero velocity [54]. This allowed a level particle bed to be maintained while avoiding spurious effects caused by particles impacting with finite velocity. However, this technique is more difficult to implement and adds the expense of finding the correct location to place the particles.

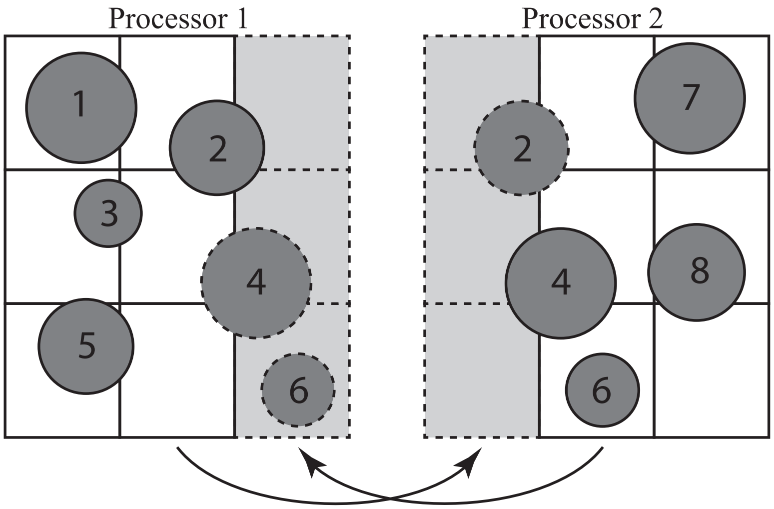

Figure 3.2 Diagram showing decomposition of domain into cells and the partitioning of cells between processors. The group of cells on the left belong to one processor, and the group on the right belong to a second processor. The particles and cells drawn with dashed lines are the ghost particles and cells as discussed in the text. The arrows represent the necessary inter-processor communication and the numbers are the particle indices.

In this work a technique is desired that allows the use of standard periodic boundary conditions while still avoiding spurious fluctuations. A new technique is developed where standard periodic boundary conditions are used in addition to a region where an artificial viscous force is added to the particles. The viscous force is chosen to be similar to an aerodynamic drag force

$$F_v \propto |\boldsymbol{v}_i|\boldsymbol{v}_i \tag{3.18}$$

where the proportionality constant determines the terminal velocity of the particle. In the following cases, the constant is chosen such that the terminal velocity is approximately twice the mean velocity of the particles in the channel. This allows the re-entering particles to catch up to the particles in the channel, while slowing them down before impacting the top of the bed. This avoids spurious fluctuation velocities in the channel, while being very easy to implement and requiring minimal computational expense.

3.2.6 Linked cell algorithm and parallelization

In order to avoid $O(N_p^2)$ operations required by Eq. 3.3, where N_p is the total number of particles, a linked cell algorithm is used [56, 59, 62]. The computational domain is decomposed into rectangular (2-D) or rectangular prism (3-D) cells as shown in Fig. 3.2. A particle is said to belong to a cell if its center lies within the cell. If the size of the cell in any direction is larger than the largest particle diameter, it is ensured that particles can only interact with other particles in their cell or in the immediately neighboring cells. Therefore, the force summation in Eq. 3.3 can be restricted to the smaller region surrounding each particle and the numerical complexity is reduced to $O(N_p)$.

Additionally, the linked cell algorithm lends itself readily to parallelization as described in Ref. [62]. Each processor is assigned a group of cells and therefore a subsection of the domain. This allows the same algorithms to be used by each processor on its sub-domain. However, care needs to be taken at the processor boundaries where particles in neighboring sub-domains can interact with particles within the processor's domain. In order to handle these inter-processor collisions, the particle information for the neighboring cells are shared with each processor and stored as "ghost" particles as shown by the grey shaded cells in Fig. 3.2. In this way, each processor can compute all necessary forces independently of the other processors. The only information that needs to be shared at each time step is the movement of a particle from one sub-domain to another and the updated ghost particle information at the boundaries between the two sub-domains.

The parallel algorithm was tested on case with $N_p = 40,000$ and shows very linear scaling up to 32 processors. For a larger simulation with more particles, liner scaling to a larger number of processors is expected.

3.3 Model validation

Before using the DEM methodology described above to simulate the particle curtain in Ref. [2], the granular channel flow experiment in Ref. [3] is used as a benchmark to validate the model.

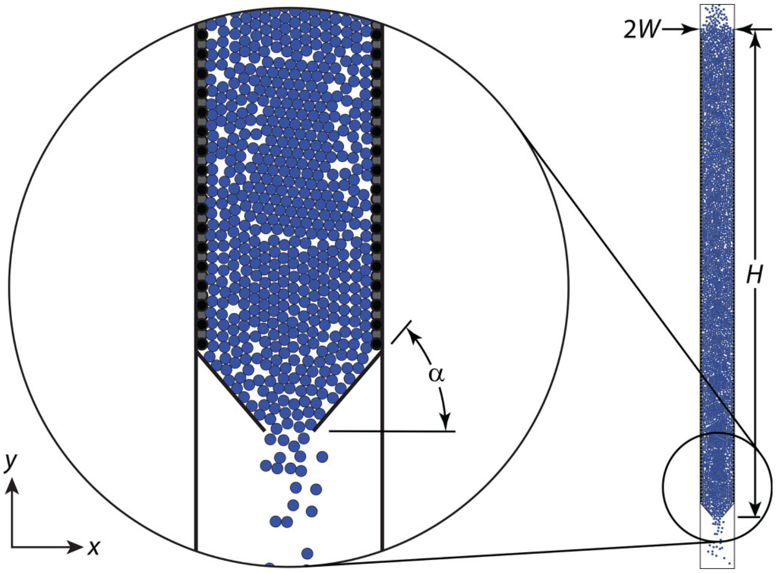

Figure 3.3 Diagram showing the geometry of the DEM simulation of the vertical channel. The dimensions for the height H, half-width W, and hopper angle α are shown. The particles at the wall are fixed particles used to create a rough wall condition. In smooth wall cases, these are absent.

3.3.1 Setup

The details of the experiment by Natarajan *et. al.* are as follows. The dimensions of the channel are height $H = 100$ cm, width $2W = 5$ cm, and depth $d = 2.18$ cm. The front and back walls are polished glass to replicate a 2-D flow. Two wall conditions are used for the side walls. A smooth wall condition is created using polished glass and a rough wall using particles glued to the walls in an approximately hexagonal close packed configuration. The particles are glass beads with a mean diameter of $D = 3$ mm with a standard deviation of 2.13 %. A feed hopper is used to feed particles into the channel. At the bottom of the channel is a flow control valve with variable width. This work will focus on the data obtained for a slit width of 1.3 cm.

Numerically, the setup shown in Fig. 3.3 is used. The width and depth of the domain are matched to the experiment. Instead of a feed hopper, periodic boundary conditions are used as described in Section 3.2.5 to create a steady flow of particles. The flow control valve geometry was not specified in the experiment, therefore a hopper design with angled walls is used where the angle α is determined as described in Section 3.3.2 below. Additionally, the 2.18 % standard deviation in the particle diameter is matched numerically. A Gaussian distribution is chosen, however it is cutoff at two standard deviations to prevent small particles from overly restricting the time step and large particles from restricting the cell size for the linked-cell algorithm. Similar cutoffs have been used previously in numerical simulations [59].

The polished glass walls are modeled as planes with the same properties as the glass particles. For the rough wall case, fixed particles are arranged in a hexagonal close packed arrangement at the wall.

The particle properties are chosen to match the properties of glass as used in the experiment. The specific type of glass used was not mentioned, however glass is known to have a density of 2400–2800 $\mathrm{g/m^3}$. The value used in the simulation is determined as described in Section 3.3.2 below. The friction and restitution coefficients for binary collisions between small glass spheres have been measured as $e = 0.97$ and $\mu = 0.092$ [84]. Additionally, the elastic modulus is 60×10^9 Pa and Poisson's ratio is 0.24 [85].

The coordinate system is shown in Fig. 3.3 with the y-axis pointing upward in the streamwise direction, x-axis in the transverse direction, and the z-direction along the depth of the channel. The $x = 0$ location is the centerline of the channel. The velocity components in the x and y directions are u and v, respectively.

3.3.2 Model calibration

One parameter that is left to be determined is the height of channel H, and resulting N_p, that is required. It has been observed experimentally that, contrary to the behavior of a liquid, the pressure at the bottom of a hopper becomes independent of H above a critical height because the weight of the particles is supported by the sidewalls [55]. In testing what this critical height is, a simulation is performed where the periodic boundary conditions are not used, causing the particles to drain out of the hopper and not re-enter. Therefore H steadily decreases and the mass flow rate $\dot{m}$ is measured as a function of H. An example of the results obtained is shown in Fig. 3.4. In this figure, it is evident that above $H \approx 0.2$ m the mass flow rate becomes constant. In the final simulations, $H = 0.75$ m is used, which is still small enough to compute in a reasonable time and is well above the critical height.

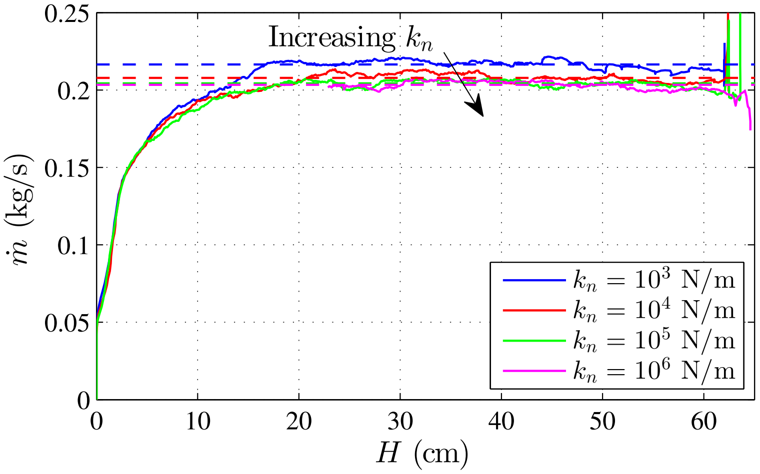

Figure 3.4 (Color online) Plot of mass flow rate $\dot{m}$ versus height H for various values of spring stiffness k_n.

The next parameter that needs to be determined is the normal stiffness, k_n, for the spring model. If k_n is chosen to accurately match the elastic modulus of glass particles, the equations become impractically stiff and expensive to solve. For example, using the relation between k_n and the elastic modulus given in Ref. [86] with a characteristic velocity of 1 m/s, $k_n = 2.1 \times 10^6$ N/m would be required. In many cases it is possible to use a smaller k_n than would be needed to match the material properties, because the large scale flow features become independent of k_n in the limit of large k_n. A range of simulations are run at various k_n to determine when the solution properties of interest (mass flow rate $\dot{m}$, mean transverse and streamwise velocity components $\langle u \rangle$ and $\langle v \rangle$, and fluctuation transverse and streamwise velocity components u' and v') become independent of k_n. Here the angle brackets denote an averaged quantity, and the prime indicated the standard deviation. Figure 3.4 shows the change in $\dot{m}$ with k_n. As evident, from this figure, $\dot{m}$ becomes independent of k_n at $k_n = 1 \times 10^5$ N/m. Although not presented here, the same trend is observed in the other flow properties of interest $\langle u \rangle$, $\langle v \rangle$, u', and v'. Therefore $k_n = 1 \times 10^5$ N/m is the value used in the remainder of the simulations.

As mentioned in the previous section, the type of glass used for the particles (and therefore density ρ) and the angle α of the hopper walls is not specified in Ref. [3]. Therefore, these

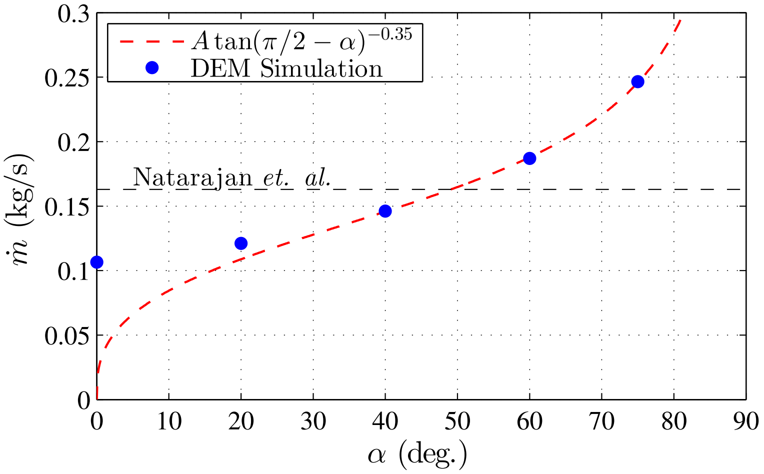

Figure 3.5 (Color online) Plot of $\dot{m}$ versus α. Data from this work are shown in filled symbols and the fitted empirical relation is the red dotted line. The horizontal dotted line is the experimentally measured $\dot{m}$.

parameters are chosen as fitting parameters to match to the mass flow rate $\dot{m}$ and mean streamwise velocity $\langle v\rangle$ measured in the experiment. In order to determine the angle dependence of $\langle v\rangle$ (and $\dot{m}$ which is proportional to $\langle v\rangle$) on the hopper exit angle α, a number of cases were simulated with varying α. The results are plotted in Fig. 3.5. Experiments have shown empirically that

$$\dot{m} = A[\tan(90^\circ - \alpha)]^{-0.35}, \tag{3.19}$$

is a good fit to the dependence of $\dot{m}$ on α, where A is the constant of proportionality [53]. This relation is only valid in the "mass flow" regime where there is no stagnant region near the hopper base, therefore it is only valid for $\alpha \gtrsim 45^\circ$. The two largest α data points in Fig. 3.5 are fitted using least-squares by Eq. (3.19) which yields $A = 0.149$ kg/s and the resulting fit is plotted as a dashed line in Fig. 3.5. It is evident that the numerical simulations agree well for large α. By validating the angle dependence with the relation in Ref. [53], it allows interpolation to choose the correct α to match the conditions in Ref. [3]. Since it is observed that $\langle v\rangle$ is weakly dependent on ρ, and $\dot{m} \propto \langle v\rangle$, the hopper angle α is interpolated using Eq. (3.19) in order to match the $\langle v\rangle$ observed in Ref. [3]. Then, ρ is chosen in order to also match the $\dot{m}$ observed in the experiment. Using this process, the final ρ is 2600 kg/m^3 and

Table 3.1 Physical properties of the particles used in the simulations.

Property	Symbol	Value	Units
Density	ρ	2600	kg/m^3
Poisson's Ratio	ν	0.22	
Restitution Coefficient	e	0.97	
Friction Coefficient	μ	0.092	
Radius	R	1.5	mm
Normal Stiffness	k_n	1×10^5	N/m

the final α is determined to be 49.4°. Given the density range of glass given in the previous section, both these values are in the expected range.

The final properties of the particles used in the numerical simulations are given in Table 3.1.

3.3.3 Results

With ρ and α calibrated to match the experimentally measured $\dot{m}$ and $\langle v \rangle$, the simulation can be compared with the experimental measurements. The first step is computing the velocity profiles. In the experiment, the velocity of the particles are computed by tracking the displacement of a particle over images taken at a rate of 30 fps. The same technique was used to compute the velocity in the DEM simulations. In addition, the statistics of the velocity, such as the mean and standard deviation, need to be calculated as a function of location within the channel. In the experiment, bins were used and the velocities were averaged over all particles that pass through the bin. A particle is defined to be in the bin if its center is within the bin. Reference [3] used bins 0.5D wide by 2 cm high. It was found in the DEM results that using a bin 0.5D wide lead to bin-to-bin oscillations in the statistics due to the layering of particles near the boundary. In other work, bin sizes around 1.0D to 1.5D are often used [67, 65, 87]. Much smoother statistics are obtained with bins 1.5D wide, therefore this is the size used in the plots below.

Simulations are performed for both smooth wall and rough wall cases. The smooth wall results are given in Fig. 3.6. Note that the data from Natarajan *et. al.* was only reported for half of the channel. In the figures presented here, the data are mirrored about the channel

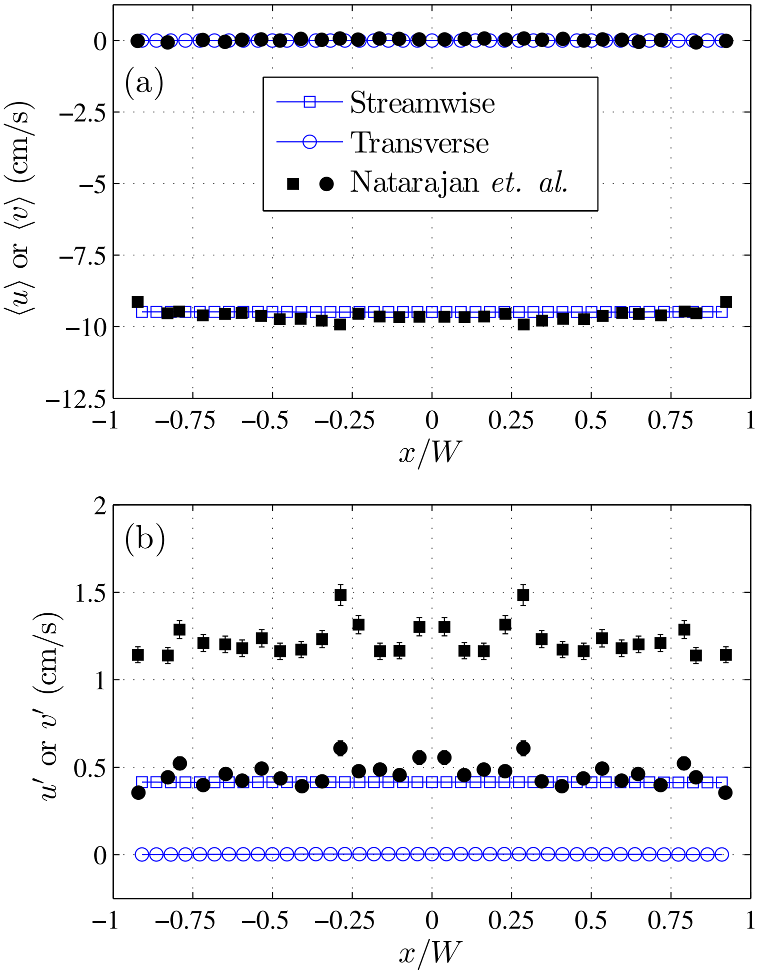

Figure 3.6 (Color online) Velocity profiles for the smooth-walled channel. Plots are included of (a) the mean velocity components $\langle u \rangle$ and $\langle v \rangle$ and (b) the fluctuating components u' and v'. Open symbols are data from this work and filled symbols are data from Natarajan *et al.* [3]. Squares are the streamwise component of velocity u and circles are the transverse component v.

centerline. The error bars on the fluctuating velocity components represent the 4% and 7% error in the streamwise and transverse components, respectively, as reported in Ref. [3].

As seen in these results, a flat profile is correctly predicted, and the magnitude of the mean velocity in both the streamwise and transverse directions are correct. Looking at the results for the fluctuation velocity in Fig. 3.6b, it is apparent that in both the streamwise and transverse directions, the fluctuation magnitude is significantly under-predicted.

In the simulation of the rough walled channel, the calibration of α lead to a slightly different value of $\alpha = 54.2°$ in order to match the experimentally measured $\langle v \rangle$ at the centerline. The velocity profiles obtained for the rough wall case are plotted in Fig. 3.7. In Fig. 3.7a, the mean velocity profile is shows good agreement with the experiment. The transverse component of the fluctuation velocity in Fig. 3.7b also shows reasonable agreement. However, some discrepancy between our simulation and the experimental data is observed in the streamwise fluctuation velocity. The fluctuations near the wall are correct, however the simulation is predicting much lower fluctuations in the center of the channel than was measured experimentally.

In the hope of obtaining results that more closely match the experiment, the friction and restitution coefficients are varied in order to see the dependence of the velocity profile on these quantities. As discussed in Appendix B below, varying these parameters did not yield improved agreement with the experimental data.

Another possible cause of the disagreement in the steamwise fluctuation is the simplified friction model Eq. 3.16 that is being used as opposed to the full linear friction model in Eq. 3.12. We compared these two models by running both smooth and rough-walled channel cases using the open source DEM code LIGGGHTS [88] using the same particle properties. The results are compared with the results from this work in Figs. B.3 and B.4 of Appendix B. For the smooth-walled channel, slightly better agreement is obtained for v', and in the rough-walled channel, slightly better results are obtained near the walls for $\langle v \rangle$ with the full linear model, however overall very similar results are obtained. These observations confirm those found in Ref. [62] where they observed that the simplified model in Eq. 3.16 is a good compromise between accuracy and cost for granular flows dominated by sustained contact between particles.

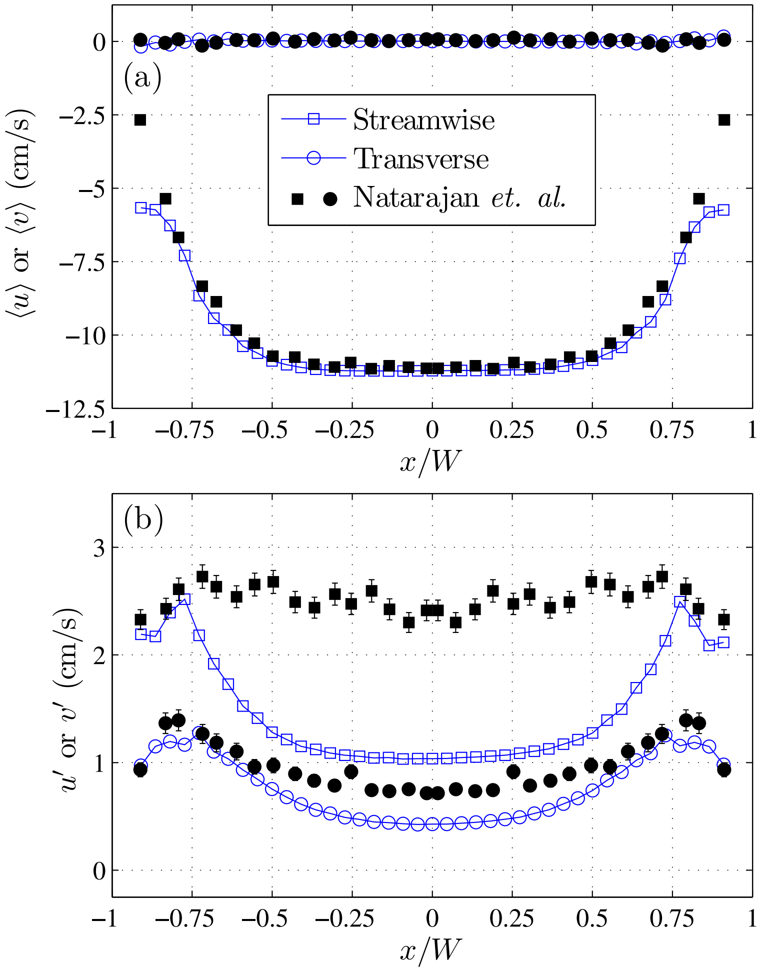

Figure 3.7 (Color online) Velocity profiles for the rough-walled channel. Plots are included of (a) the mean velocity components $\langle u \rangle$ and $\langle v \rangle$ and (b) the fluctuating components u' and v'. Open symbols are data from this work and filled symbols are data from Natarajan *et al.* [3]. Squares are the streamwise component of velocity u and circles are the transverse component v.

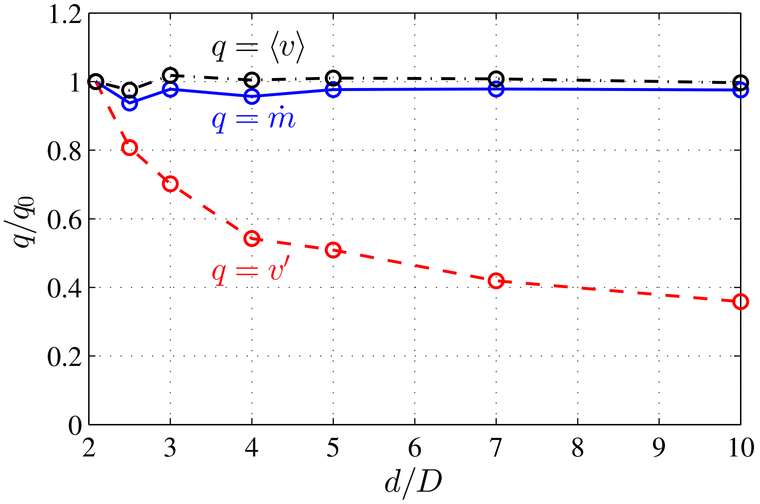

Figure 3.8 (Color online) Plot of $\langle v \rangle$, $\dot{m}$, and v' versus the nondimensional periodic depth in the z-direction d/D. All quantities are normalized by q_0 which represents the value at the smallest d/D.

Although, the shape of the $\langle v \rangle$ profile in Fig. 3.7 is very different from that obtained by Natarajan *et. al.*, other similar experimental work has yielded a qualitatively similar shape in fluctuation velocity. For example, Fig. 4d in Ref. [43] shows a very similar profile with a peak in fluctuations near the walls and a minimum at the center of the channel, as opposed to the relatively flat profile obtained by Natarajan *et. al.* The source of these qualitative differences is not clear. Overall, the results of the vertical channel flow validation show that with careful choice of model parameters, the DEM approach is useful for the prediction of the properties of granular flows with reasonable accuracy.

3.3.4 Periodic depth dependence

In the particle curtain that will be discussed next, the depth of the curtain in the z-direction (referring to the same coordinate system as the channel above) is large compared to its width. Therefore, numerically it can be considered semi-infinite and simulated using periodic boundary conditions on the z boundaries. However, it is unclear how large of depth d in the periodic direction needs to be simulated. Therefore, before the curtain is simulated, simulations of the vertical channel case at various d are performed. The steady-state mean and fluctuation

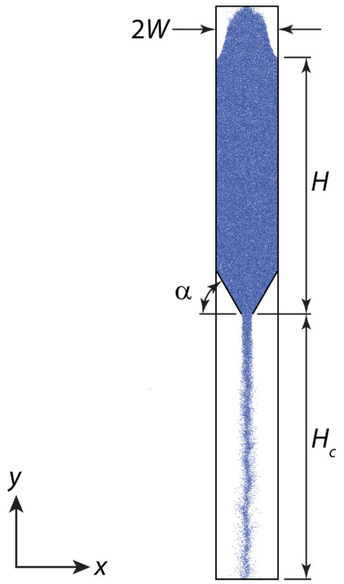

Figure 3.9 Geometry of the numerical simulation of the particle curtain. The origin is at the center of the slit opening where the particle curtain begins.

velocities in the streamwise direction as well as the mass flow rate for the smooth-wall case are tracked as a function of d. The results are plotted in Fig. 3.8. It is observed that the mean velocity and mass flow rate are relatively independent of d, however the fluctuation velocity is strongly dependent until around $d = 10D$ where D is the mean particle diameter. In the next section, a depth of $10D$ is used when simulating the particle curtain.

3.4 Particle curtain predictions

Given the good agreement between our DEM simulations and the experimental results for the vertical channel flow, we proceed to simulate the particle curtain in Ref. [2]. A discussion of the geometry and model parameters will be discussed next, followed by the results.

3.4.1 Setup

The geometry of the problem is shown in Fig. 3.9. The width of the hopper is $2W = 17.8$ mm and the slit opening is 3.2 mm wide. The walls at the bottom of the hopper are angled at $\alpha = 60°$ with respect to horizontal. The visible length of the particle curtain is $H_c = 76.2$ mm and the particles are glass spheres with diameters sorted to 106–125 μm. For a full description of the experiment, see Ref. [2].

The particle diameters are chosen to have a Gaussian distribution with a mean of 115.5 μm and standard deviation of 4.75 μm. The distribution was cut off at two standard deviations to give the correct diameter bounds of 106 μm and 125 μm. From the channel flow simulations it is determined that for a height above $4(2W)$, the mass flow rate becomes independent of height. Therefore, the height of particles in the feed hopper is chosen such that $H \geq 71.2$ mm for this particle curtain simulation. The depth in the periodic z-direction must be $d \geq 10D$ for the solution properties to be independent of d as determined in Section 3.3.4. Using the mean particle diameter, this requires $d = 1.155$ mm. All particle properties except for k_n (which is discussed below) are the same as those used in the channel flow simulation given in Table 3.1 above because glass particles are being simulated in both cases.

For post processing the statistics of the particle curtain, the same bin-wise averaging as above is used. In this case, the bin dimensions are chosen to be $2D$ by $10D$ in the x and y directions, respectively. In calculating the solid volume fraction of a bin, the total volume of the spheres whose centers lie in the bin is divided by the total bin volume. This value is then time averaged. The errors associated with particles overlapping the edges of the bin are averaged out through the time averaging process.

3.4.2 Results

The above geometry requires approximately 1.5 million particles to be simulated. The high computational cost and limited resources demand that the time step size (determined by N) and spring stiffness k_n be chosen judiciously to satisfy accuracy of the solution and computational cost. Simulations are first performed at various N and the results are presented and discussed in Appendix C. $N = 15$ is chosen because although the results are not completely convergent, the error is estimated to be less than 5 % for all relevant quantities. The stiffness k_n was chosen to be 32 N/m as this is the largest that could be simulated given the resources available. Any errors associated with simulating overly soft particles is discussed following the presentation of the results.

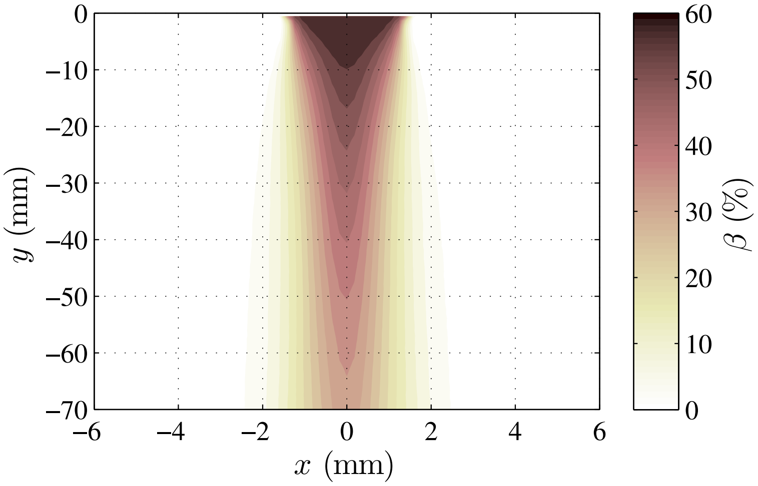

Figure 3.10 (Color online) Contour plot of the mean volume fraction β in the particle curtain.

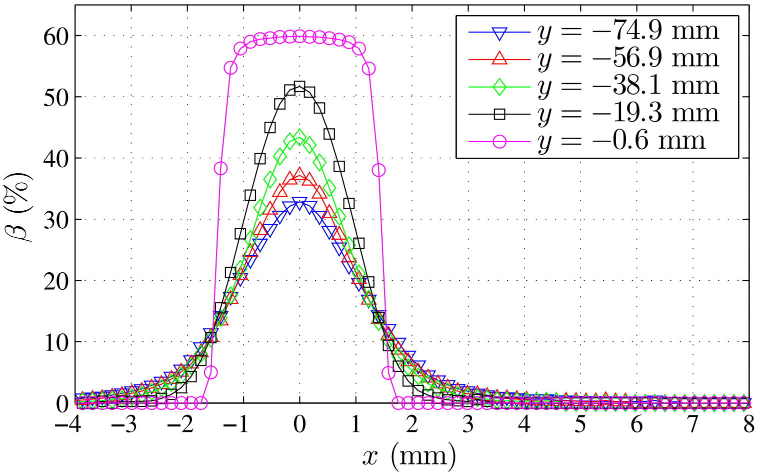

Figure 3.11 (Color online) Volume fraction β versus x at various y locations in the particle curtain.

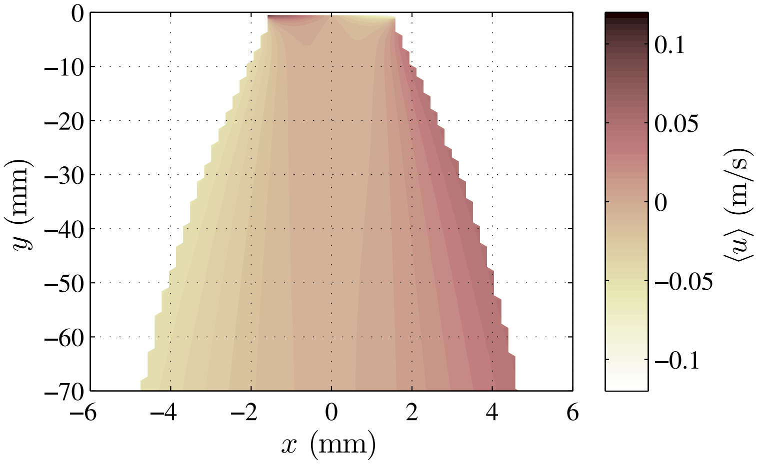

Figure 3.12 (Color online) Contour plot of the horizontal component of the mean velocity $\langle u \rangle$.

The averaged solid volume fraction β contour plot for the particle curtain is given in Fig. 3.10 and cuts at various y locations are shown in Fig. 3.11. It is evident that immeditaely after the particles leave the slit opening, β is a nearly uniform 60 % across the width of the curtain. The theoretical maximum β for spheres of equal sizes is 74.05 %, and the random close packing limit has been observed to be 60–68 % [89].

By the time the particles reach $y = -19.3$ mm, the relatively flat β profile has become Gaussian-like. As the particles continue to fall further from the slit opening, the evolution of the β profile is mostly characterized by the dilation due to the gravitational acceleration. At the midpoint of the curtain ($y = -38.1$ mm) the volume fraction at the centerline is 43 % and the curtain is approximately 4 mm wide. The wording in Ref. [2] suggests a relatively uniform β across the width of the curtain. Although this is observed immediately after the particles exit the curtain, for the bulk of the curtain a highly non-uniform, Gaussian-like, profile is observed in this work.

A look at the mean velocity profiles for the $\langle u \rangle$ and $\langle v \rangle$ velocity components in Figs. 3.12 and 3.13, respectively, explain the behavior of β. At the top of the curtain, there is a very thin region where the $\langle u \rangle$ velocity points inward caused by the angled side walls that form the slit opening. This inward velocity causes the β profile to be pushed toward the center and become nonuniform. Below this region, there is a wide portion of $\langle u \rangle \approx 0$ in the center of the curtain

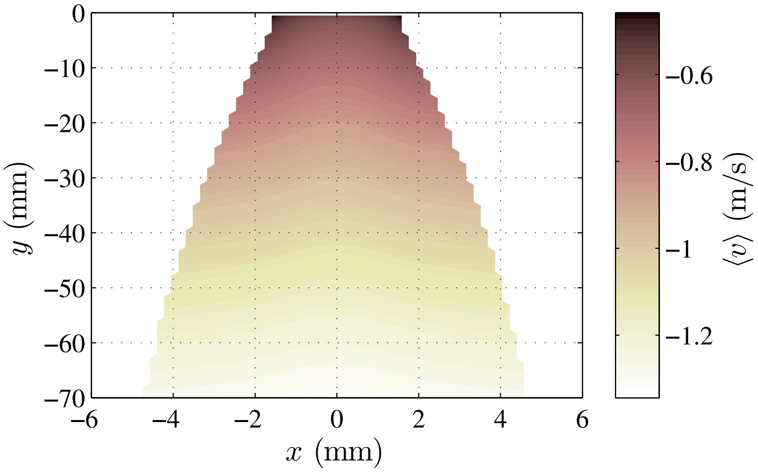

Figure 3.13 (Color online) Contour plot of the vertical component of the mean velocity $\langle v \rangle$.

with the outer edges having velocities pointing outward. This explains the relatively constant shape of the β profiles observed everywhere outside the thin region at the top of the curtain. Note that these velocity contours are only shown on the bins that have at least 10 particles to average over.

Additionally, it is interesting to look at the contour plots of the fluctuation velocities u' and v' in Figs. 3.14 and Figs. 3.15, respectively. In both plots, there is a very thin region near the hopper exit where there are relatively large fluctuation velocities. However, outside of this region the fluctuations are small. This explains the lack of "diffusion-like" spreading of the β profile.

However, comparison with the data from Ref. [2] reveals some striking discrepancies. The experiment estimated $\beta = 21 \pm 2\,\%$ and observed a curtain width of 2 mm at the midpoint of the curtain. In Fig. 3.10, the data at $y = -38.1$ mm predict a much wider curtain and β at the center more than double the experimentally observed estimate. Additionally, private communication with the corresponding author of Ref. [2] revealed that the numerically simulated mass flow rate is approximately double what is observed experimentally. It is believed that these discrepancies are caused by the overly soft nature of the particles in the simulation.

In order to assess the impact of using a small particle stiffness, simulations using even smaller values of k_n are shown in Fig. 3.16. Note that these data are taken at $y = -38.1$ mm

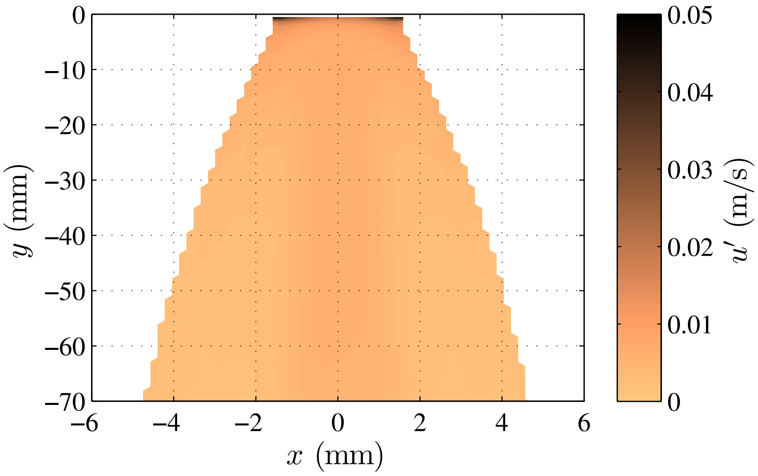

Figure 3.14 (Color online) Contour plot of the horizontal component of the fluctuation velocity u'.

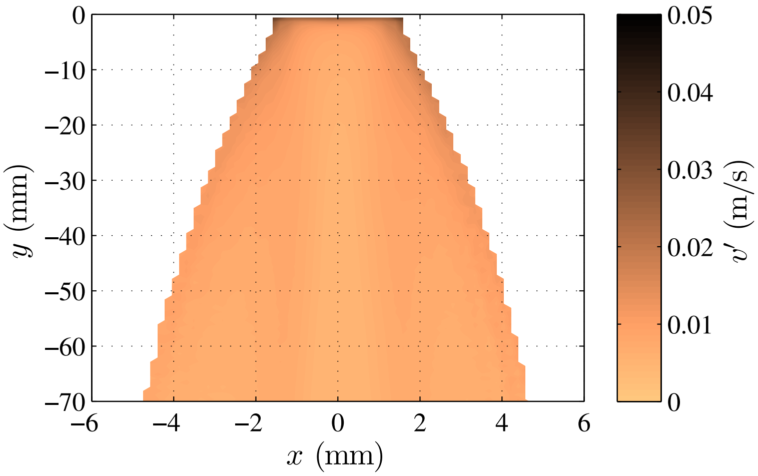

Figure 3.15 (Color online) Contour plot of the vertical component of the fluctuation velocity v'.

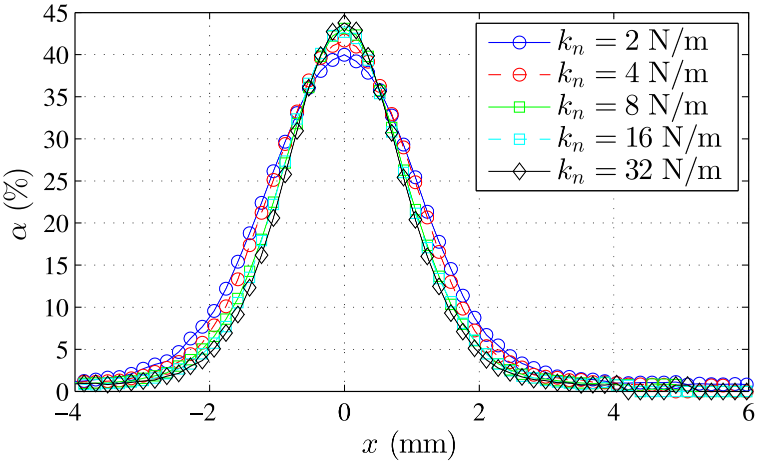

Figure 3.16 (Color online) Volume fraction β versus x at $y = -38.1$ mm for various k_n.

and are simulated for a narrower domain of $d = 3D$. These data reveal that as k_n is increased, the predicted particle curtain becomes narrower. If the particles were the correct stiffness, one could reasonably expect the simulated curtain to be closer to the 2 mm width that is observed experimentally.

3.4.3 Soft particle effects

The effect of overly soft particles on the magnitude of the flow quantities can be tested by revisiting the channel flow simulation discussed in Section 3.3. It is shown that using $k_n = 1 \times 10^5$ N/m and $N = 50$ results in accurate predictions of the flow. However, if $N = 15$ is used and k_n is decreased, the effect on the simulated results can be observed.

Starting with the same material properties and geometry as used in the final results presented in Section 3.3.3, α was changed to 60° in order to match α that is used in the particle curtain. A baseline, fully-resolved, case is run with $k_n = 1 \times 10^5$ N/m and $N = 50$. Then N is changed to 15 and k_n is decreased holding all other parameters constant in order to replicate the same level of under-resolution and particle softness that is present in the particle curtain case. The percent error of the steady mass flow rate $\dot{m}$, average streamwise velocity $\langle v \rangle$, and volume fraction β immediately below the hopper exit are shown in Fig. 3.17. Note that for all

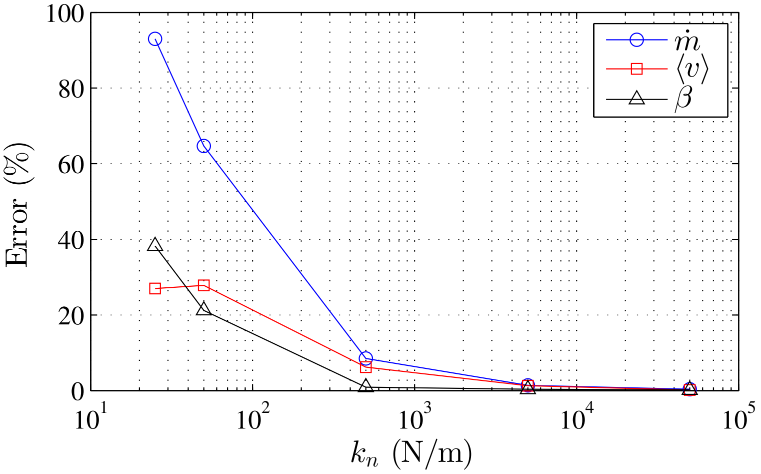

Figure 3.17 (Color online) Percent error in $\dot{m}$, $\langle v \rangle$, and β versus k_n for the channel flow case discussed in Section 3.3 above. All results are for $N = 15$ and the error is calculated based on a simulation with $k_n = 1 \times 10^5$ N/m and $N = 50$. A positive error indicates the magnitude is larger than in the fully-resolved case.

quantities, a positive error signifies that the quantity has a larger magnitude than the accurate case using $k_n = 1 \times 10^5$ N/m and $N = 50$.

As seen in Fig. 3.17, by choosing a low k_n it is possible to get a $\dot{m}$ that is nearly double the properly resolved case. Additionally, β and $\langle v \rangle$ are also 38 % and 27 % over-predicted, respectively in the case with the softest particles. Interestingly, although not presented here, $\beta = 60\,\%$ at the hopper exit for the softest-particle case, which is nearly the same as predicted in the particle curtain case in Fig. 3.11. This also agrees with the fact that an accurate prediction of β at the hopper exit should be less than the random close packing limit of 60–68 % because of the dilation that is required for movement. These results give some indication that the particles in the curtain simulation are significantly softer than necessary for quantitative predictions.

If we assume that similar error magnitudes are present in the particle curtain case, namely 38 % and 27 % too large for β and $\langle v \rangle$, respectively, we can apply a correction to the volume fraction profiles in Fig. 3.11. The dilation effect caused by the gravitational acceleration is accounted for by assuming free-fall acceleration of the particles. The scaled data are shown in Fig. 3.18. The scaled data show that β at $y = -38.1$ mm has the potential to be much lower

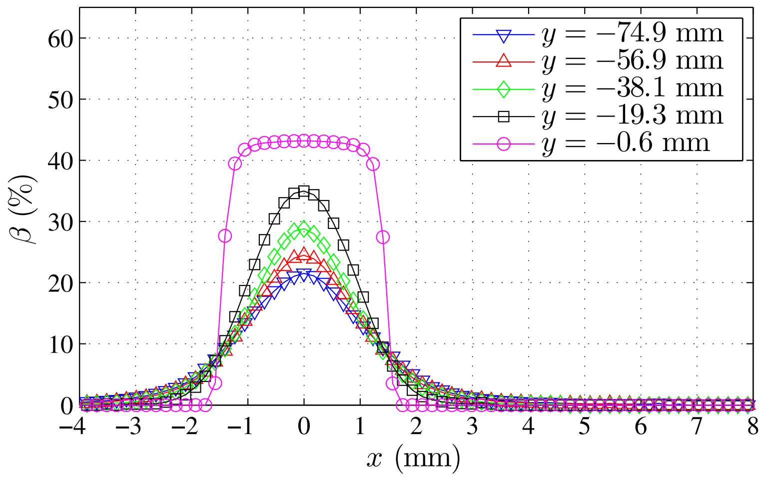

Figure 3.18 (Color online) Volume fraction β versus x at various y locations in the particle curtain. These data are scaled to the expected values if β and $\langle v \rangle$ at the hopper exit in the simulated results are 38 % and 27 % too large, respectively.

than the current simulation with overly-soft particles indicates, and the average may in fact be similar to to $\beta = 21 \pm 2\,\%$ that is cited in Ref. [2] if the correct stiffness is used.

Despite the errors caused by overly soft particles in the simulations that limit the quantitative accuracy of this data, the qualitative trends are not expected to change if the correct stiffness were used. Therefore, the results presented above still provide valuable insight into the properties of the particle curtain in Ref. [2].

3.5 Summary and conclusions

The goal of this work is to better understand the properties of the particle curtain in Ref. [2]. To simulate the granular flow from a feed hopper through a slit opening, the discrete element method is used. The linear-spring and dashpot model is used for the normal component of the collisional force and a static friction model is used for the tangential component. In order to simulate a steady flow of particles through the domain, periodic boundary conditions are used in conjunction with a novel damping force that slows re-entering particles to avoid spurious fluctuation velocities.

To validate our DEM model, we first simulate a granular channel flow and compare with the experimental results in Ref. [3]. The profiles of the mean and fluctuating components of both the streamwise and transverse velocity components within the channel are compared. Both smooth and rough wall conditions are tested. In both cases, the mean velocity show excellent agreement with the experiment. The smooth wall case under-predicts both components of the fluctuation velocity. However, in the rough-wall case, the transverse fluctuation velocity is well predicted. The streamwise fluctuation velocity in the rough wall case shows some disagreement in the center of the channel, but qualitatively agrees with the results from similar experiments.

Finally, the properties of the particle curtain in Ref. [2] are examined. Contrary to indications from the experimental results, the DEM simulations show a Gussian-like volume fraction profile across the width of the curtain. The behavior of the particle curtain is governed mostly by free-fall. The fluctuation velocities are mostly confined to the region near the hopper exit and are observed to quickly decay as the particles fall.

Comparison with the data in Ref. [2] indicates that the DEM results have error believed to be caused by the simulated particles being overly soft. Error analysis suggests that results using a larger stiffness would show better agreement with the curtain width, volume fraction, and mass flow rate that are observed experimentally. This also highlights the importance of modeling particles with adequate stiffness to produce quantitative flow predictions.

CHAPTER 4. GENERAL CONCLUSIONS

4.1 General discussion

The goal of this work is the development of tools for the simulation of gas-solid multiphase flows. Specifically, this work is applied to the simulation of a shock wave impacting a particle curtain as tested experimentally in Ref. [2]. Due to the high Reynolds numbers, high particle volume fraction, and the presence of a shock wave that exist in the flows of interest, many existing methods for simulating multiphase flows are not applicable. This work looks to fully-resolve the flow features and therefore limit the amount of modeling that is required. This means solving the complete Navier-Stokes equations for the fluid phase. An adaptive wavelet collocation method is utilized which allows a highly resolved grid to be used only in the necessary regions of the fluid. The boundaries of the particles are resolved through a recently developed volume penalization immersed boundary method. The collisions between particles are modeled using a hard sphere approximation because of its efficiency and accuracy for the flow regime that is studied. A proof of concept case is presented that showcases the abilities of this method.

Another goal of this work is the prediction of the properties of the particle curtain in Ref. [2]. Information such as the volume fraction and velocity profiles are important in order to generate an initial condition that accurately replicates the experiment in Ref. [2]. This information is obtained through a DEM simulation.

In the simulation of the particle curtain, a linear-spring dashpot is used to model the normal force and the tangential force is modeled by a static friction model. A linked-cell algorithm is used in addition to parallelization in order to increase the computational efficiency and allow the simulation of a large number of particles.

The DEM model is validated through comparison with a vertical channel flow experiment. The mean and fluctuation velocity profiles showed very good agreement with the experiment. When simulating the particle curtain, computational resources limited the particle stiffness that could be simulated. This caused some discrepancies between the simulated and experimentally observed particle curtains. However, the simulations showed that the particle curtain volume fraction varies across the width of the curtain unlike previously thought. Additionally, error analysis revealed that if the correct stiffness were used, better agreement with the experiment is expected.

4.2 Recommendations for future research

There are a few avenues for future work on this subject. The first involves the numerical method for coupling between solid and fluid phases. The current implementation is a first order accurate technique. Future work will extend this technique to be second order accurate or higher. Another area for future work is the simulation of the particle curtain. The current computational limitations did not allow for a fully resolved simulation. When more resources become available, the simulation will be able to be rerun and more accurate results can be obtained. This will allow a better quantitative analysis of the particle curtain properties. Finally the tools that have been developed in this work will allow a highly resolved simulation to be performed of the shock wave particle cloud interaction that was studied in Ref. [2]. The results of such a simulation will be invaluable in better understanding the flow features that develop in this complex regime of multiphase flows.

APPENDIX A. VALIDATION OF HARD SPHERE COLLISION MODEL

In this section, we look to provide confirmation the particle phase is obeying the principals of conservation of energy and momentum. This is achieved by simulating a system of particles and monitoring the system's total energy and momentum. In this example, a 3-D simulation of ten particles is used where periodic boundaries are applied in all three directions. By using periodic boundaries, we eliminate collisions with walls, which are an external force and therefore do not conserve the system's total momentum. Additionally, the parameters e and μ are set to unity and zero, respectively, so that no energy should be lost during the collisions. The simulation is allowed to run for a total of ten seconds, allowing many collisions between particles to occur. In the following results, only two of the ten seconds are shown for clarity.

We first look at the conservation of kinetic energy K. The systems total kinetic energy is computed with

$$K_{\text{total}} = \sum_i \frac{1}{2} m_i ||\boldsymbol{v}_i||^2 \tag{A.1}$$

where i denotes the particle index. The result is plotted in Fig. A.1. In this figure, K_{total} is periodically sampled and plotted versus time t. The vertical black lines indicate the times that a particle-particle collision occurs somewhere in the system. This result shows that even through numerous collisions, the K_{total} is conserved.

We use a similar analysis to check for conservation of momentum. Both linear $\boldsymbol{P}$ and angular $\boldsymbol{L}$ momentum need to be conserved. We compute the total linear momentum using

$$\boldsymbol{P}_{\text{total}} = \sum_i m_i \boldsymbol{v}_i. \tag{A.2}$$

The total angular momentum for the system of spheres about the origin is

$$\boldsymbol{L}_{\text{total}} = \sum_i \left[I_i \boldsymbol{\omega}_i + \boldsymbol{x}_i \times (m_i \boldsymbol{v}_i) \right]. \tag{A.3}$$

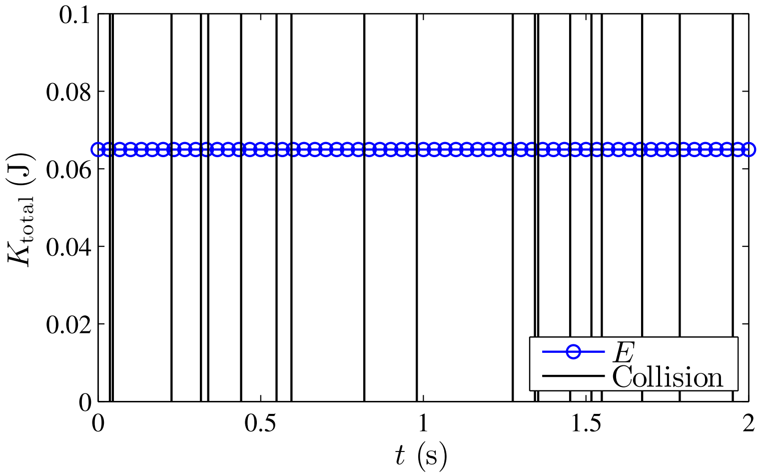

Figure A.1 Total system kinetic energy K_{total} versus time t. Vertical lines indicate the time that a particle-particle collision occurs.

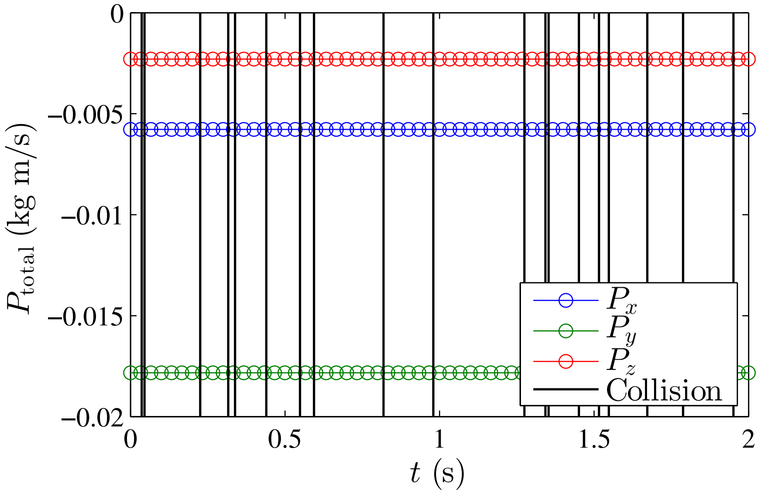

Figure A.2 Total system momentum P_{total} versus time t. Vertical lines indicate the time that a particle-particle collision occurs.

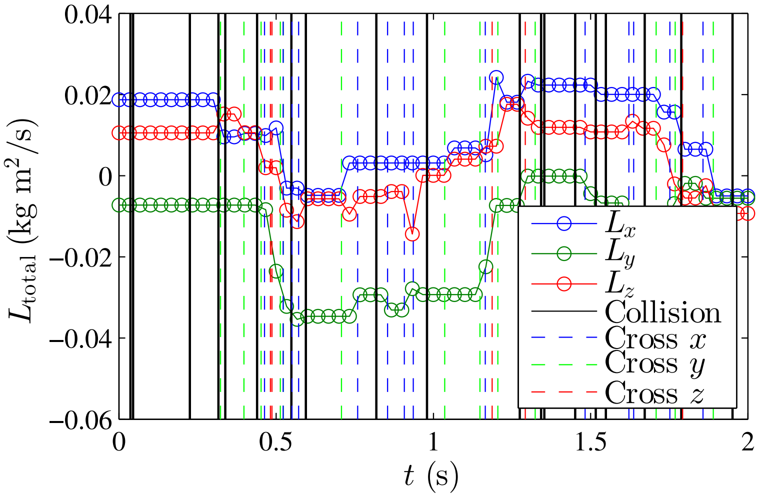

Figure A.3 Total system angular momentum K_{total} versus time t. Solid vertical lines indicate the time that a particle-particle collision occurs. The dashed vertical lines are the times that a particle crosses one of the periodic boundaries.

The results for $\boldsymbol{P}$ are plotted in Fig. A.2 and $\boldsymbol{L}$ in Fig. A.3. Note that through all collisions, all three components of $\boldsymbol{P}_{\mathrm{total}}$ and $\boldsymbol{L}_{\mathrm{total}}$ are conserved. However, in Fig. A.3, it is observed that the components of $\boldsymbol{L}_{\mathrm{total}}$ are not constant with time. This is because of the discontinuity in $\boldsymbol{x}$ when a particle crosses a periodic boundary. Therefore, the dashed vertical lines in Fig. A.3 denote the times that a particle crosses a periodic boundary. The times that this occurs, we expect to see a jump in the components of $\boldsymbol{L}_{\mathrm{total}}$ as is observed.

Although not presented here, similar cases were run with non-periodic system boundaries, gravitational forces, inelastic collisions, and frictional collisions. The conservation laws are confirmed to be obeyed in all cases that they are applicable. For example, during inelastic collisions we expect momentum to be conserved, but energy should not be. These results suggest that the collisions between particles are simulated accurately.

APPENDIX B. EFFECT OF COLLISION MODEL AND PARAMETERS

In the hope of improving the quality of agreement between the experimental and DEM results in the channel flow simulation, the friction coefficient μ and restitution coefficient e are adjusted. μ is tested in the range 0.00–0.15 and e from 0.9–1.0. The change of results with respect to μ are plotted in Fig. B.1 and with respect to e in Fig. B.2. All results are for the rough-walled channel case. Note that these results are simulated with the hopper angle $\alpha = 49.4°$ calibrated for the smooth-wall case, as opposed to the recalibrated $\alpha = 54.2°$ that is presented for the rough-walled channel in the main text.

It is evident in Fig. B.1 that changing μ has the most pronounced effect on the mean streamwise velocity $\langle v \rangle$. With decreasing μ there is an increase in $\langle v \rangle$. This is in agreement with intuition, as less friction allows particles to slide past each other more easily and therefore flow through the channel more quickly. Additionally, with decreasing μ, it is observed that u' at the channel walls increases. However, none of the results obtain a better overall result when compared to the experimentally measured values.

When changing e as shown in Fig. B.2, there is very little effect on the velocity profiles, therefore varying this parameter did not yield a better result.

Another parameter that is worth investigating is the choice of friction model. In this work, the simplified model in Eq. 3.16 is used as a compromise between accuracy and computational cost. However, it is interesting to see the effect of using the more accurate full linear friction model in Eq. 3.12. To preform this comparison, the open source code LIGGGHTS [88] is used to simulate both the rough and smooth walled channel cases. In LIGGGTS, the full linear friction model is used, but all other model parameters are kept fixed. The comparison between the LIGGGHTS results and those from this work are presented in Figs. B.3 and B.4 for the smooth and rough walled channels, respectively.

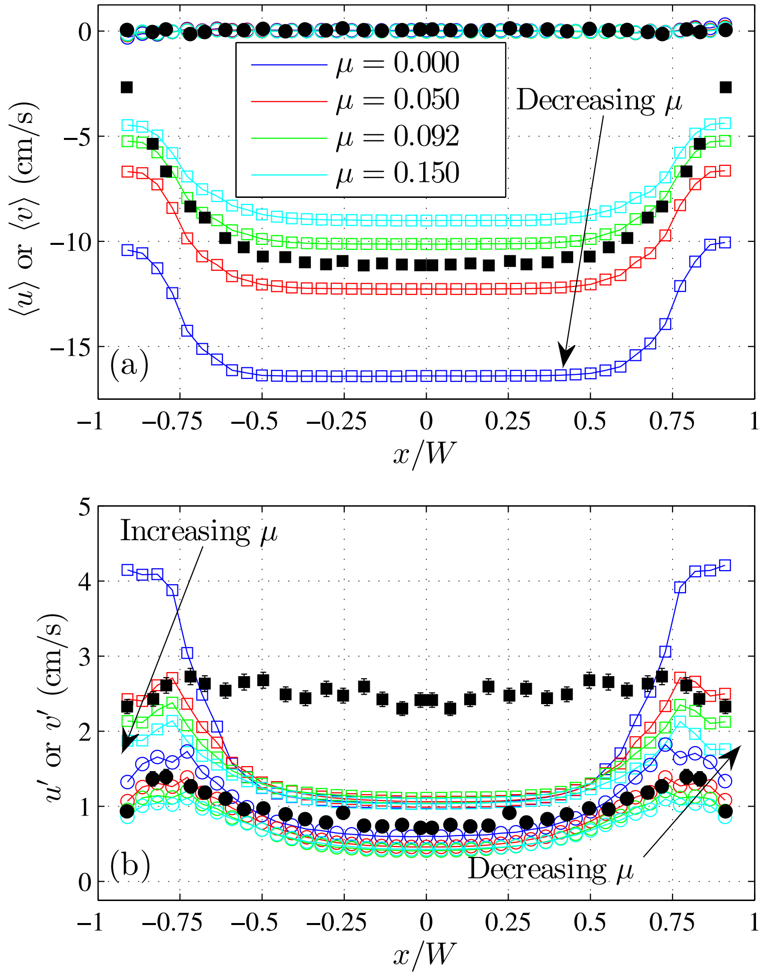

Figure B.1 (Color online) Velocity profiles for the rough-walled channel simulated at various μ. Plots are included of (a) the mean velocity components $\langle u \rangle$ and $\langle v \rangle$ and (b) the fluctuating components u' and v'. Open symbols are data from this work and filled symbols are data from Natarajan *et al.* [3]. Squares are the streamwise component of velocity u and circles are the transverse component v.

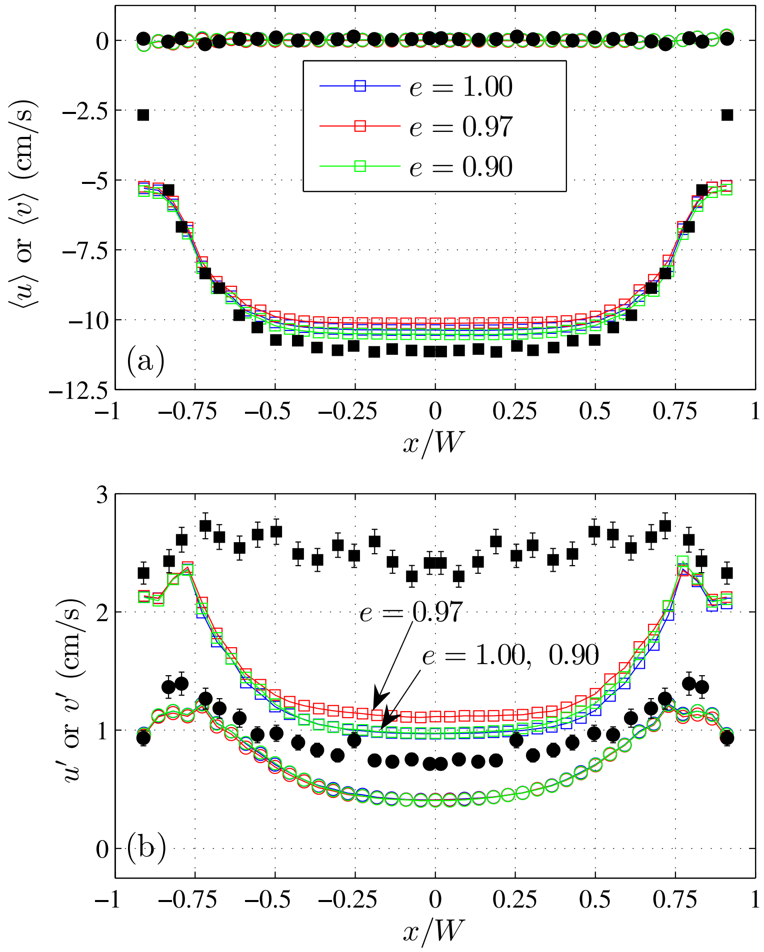

Figure B.2 (Color online) Velocity profiles for the rough-walled channel simulated at various e. Plots are included of (a) the mean velocity components $\langle u \rangle$ and $\langle v \rangle$ and (b) the fluctuating components u' and v'. Open symbols are data from this work and filled symbols are data from Natarajan *et al.* [3]. Squares are the streamwise component of velocity u and circles are the transverse component v.

It is observed that for the smooth walled channel, v' is closer to the measured value in the experiment when using the full linear friction model. However, v' remains under-predicted in both cases. The only other significant difference between the two friction models is $\langle v \rangle$ at the wall of the rough-walled channel. Slightly better agreement is observed using the full linear friction model. In general, both models produce roughly equivalent results, however the full linear model requires additional computational expense and memory.

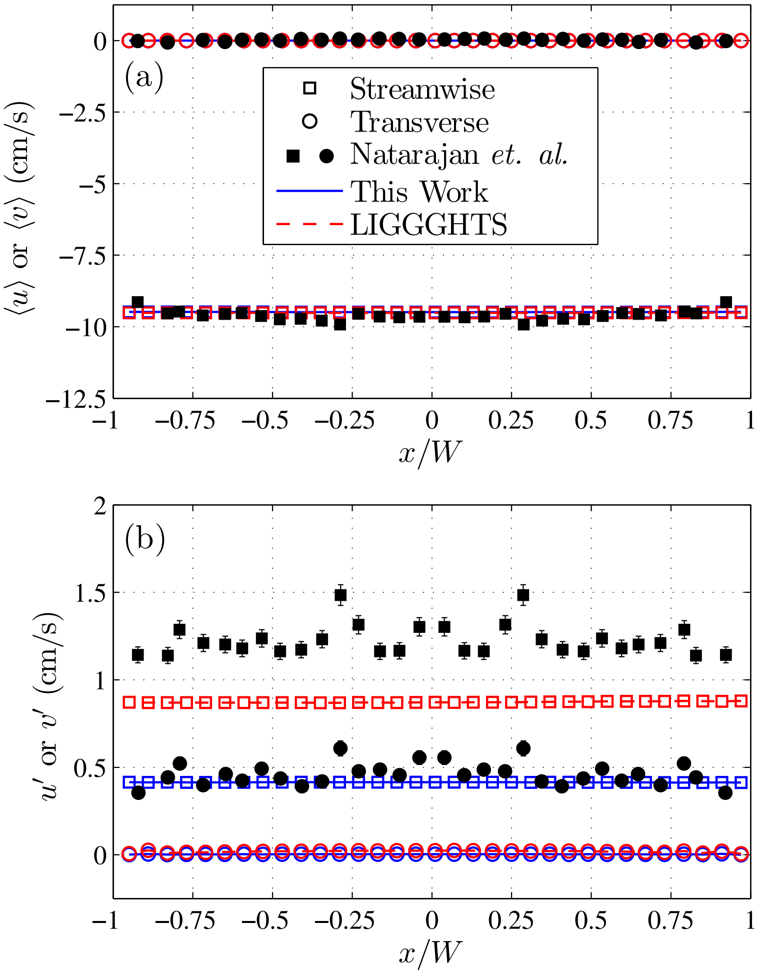

Figure B.3 (Color online) Comparison of the results from this work and LIGGGHTS for the smooth-walled channel. Plots are included of (a) the mean velocity components $\langle u \rangle$ and $\langle v \rangle$ and (b) the fluctuating components u' and v'. Open symbols are data from this work and filled symbols are data from Natarajan *et al.* [3]. Squares are the streamwise component of velocity u and circles are the transverse component v.

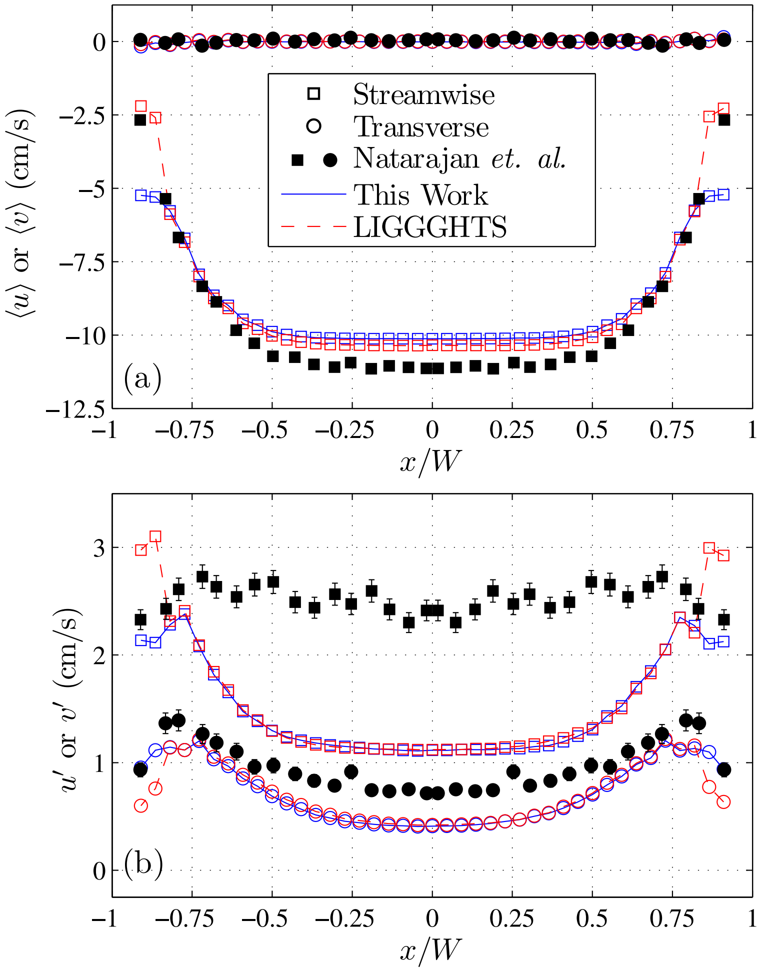

Figure B.4 (Color online) Comparison of the results from this work and LIGGGHTS for the rough-walled channel. Plots are included of (a) the mean velocity components $\langle u \rangle$ and $\langle v \rangle$ and (b) the fluctuating components u' and v'. Open symbols are data from this work and filled symbols are data from Natarajan *et al.* [3]. Squares are the streamwise component of velocity u and circles are the transverse component v.

APPENDIX C. PARTICLE CURTAIN SENSITIVITY TO N

This section looks at the sensitivity that the particle curtain properties have to N, the number of time steps per collision. $N = 7$ is the smallest value that gave convergent results, as larger step sizes do not conserve energy. The smallest step size tested corresponded to $N = 25$ and these results are used as the reference values when computing the percent error. Note that this study is performed on a smaller domain in the z-direction of $d = 3D$ as opposed to the $10D$ width used in the final simulation to save computational effort. The results for volume fraction β at $y = -38.1$ mm for each N tested are shown in Fig. C.1. It is evident from this figure that as N is increased, the only significant change is a slight increase in the peak β at the center of the curtain. All other flow quantities showed no significant change in the shape of the profiles, only slightly differing magnitudes with varying N.

We quantify the percent error of the solution by comparing the centerline value of the various flow quantities (except the mean transverse velocity $\langle u \rangle$ which is zero at the center) with the $N = 25$ baseline solution. The results are plotted in Fig. C.2. It is evident that general convergence is obtained with increasing N. Strictly due to computational resources available, $N = 15$ is chosen for the final simulations with the realization that the error in the final predictions will be on the order of $5\,\%$ due to error caused by slightly under-resolved collisions.

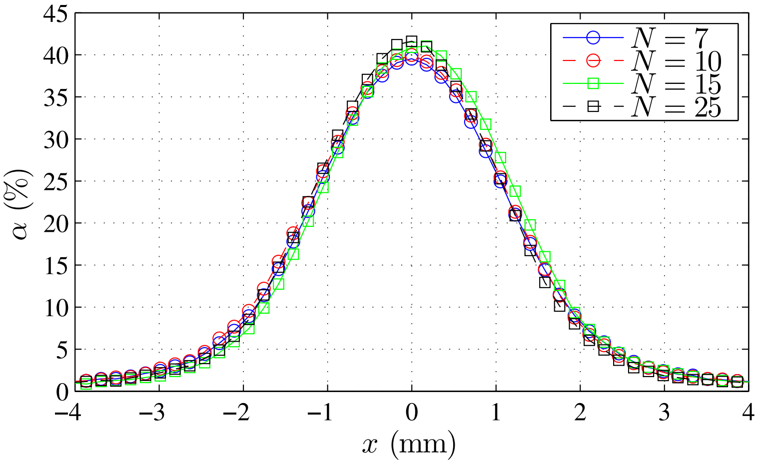

Figure C.1 (Color online) Volume fraction β versus x at $y = -38.1$ mm for various N.

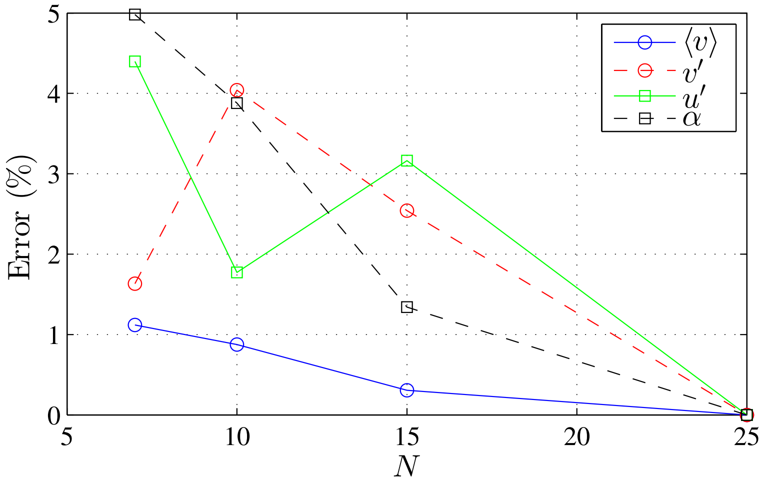

Figure C.2 (Color online) Percent error in the centerline values of the relevant solution quantities versus N at $y = -38.1$ mm.

BIBLIOGRAPHY

[1] David L. Frost, Yann Grégoire, Oren Petel, Samuel Goroshin, and Fan Zhang. Particle jet formation during explosive dispersal of solid particles. *Physics of Fluids*, 24(2012):2010–2012, 2012.

[2] Justin L. Wagner, Steven J. Beresh, Sean P. Kearney, Wayne M. Trott, Jaime N. Castaneda, Brian O. Pruett, and Melvin R. Baer. A multiphase shock tube for shock wave interactions with dense particle fields. *Experiments in Fluids*, 52(6):1507–1517, February 2012.

[3] V. V. R. Natarajan, M. L. Hunt, and E. D. Taylor. Local measurements of velocity fluctuations and diffusion coefficients for a granular material flow. *Journal of Fluid Mechanics*, 304:1–25, 1995.

[4] Z. Zhang and a. Prosperetti. A Method for Particle Simulation. *Journal of Applied Mechanics*, 70(January 2003):64, 2003.

[5] C. T. Crowe, T. R. Troutt, and J. N. Chung. Numerical Models for Two-Phase Turbulent Flows, 1996.

[6] J. H. Geng and H. Groenig. Dust suspensions accelerated by shock waves. *Experiments in Fluids*, 28:360–367, 2000.

[7] O. Igra and G. Ben-Dor. Dusty Shock Waves. *Applied Mechanics Reviews*, 41(11):379–437, 1988.

[8] X. Rogue, G. Rodriguez, J.F. Haas, and R. Saurel. Experimental and numerical investigation of the shock-induced fluidization of a particles bed. *Shock Waves*, 8:29–45, 1998.

[9] F. Zhang, D.L. Frost, P.a. Thibault, and S.B. Murray. Explosive dispersal of solid particles. *Shock Waves*, 10:431–443, 2001.

[10] A Grossmann and J Morlet. Decomposition of Hardy Functions Into. *SIAM Journal on Mathematical Analysis*, 15(4), 1984.

[11] Kai Schneider and Oleg V. Vasilyev. Wavelet Methods in Computational Fluid Dynamics. *Annual Review of Fluid Mechanics*, 42:473–503, 2010.

[12] Wolfgang Dahmen. Wavelet and Multiscale Methods for Operator Equations. *Acta numerica*, 6:55–228, 1997.

[13] Wolfgang Dahmen, Angela Kunoth, and Karsten Urban. A Wavelet Galerkin Method for the Stokes Equations. *Computing*, 56(3):259–301, 1996.

[14] Jochen Frölich and Kai Schneider. An Adaptive WaveletVaguelette Algorithm for the Solution of PDEs. *Journal of Computational Physics*, 130:174–190, 1997.

[15] L Gagnon and J M Lina. Symmetric Daubechies' wavelets and numerical solution of NLS equations. *Journal of Physics A: Mathematical and General*, 27:8207–8230, 1994.

[16] Mark Myers, Philip Holmes, Juan Elezgaray, and Gal Berkooz. Wavelet projections of the Kuramoto-Sivashinsky equation I. Heteroclinic cycles and modulated traveling waves for short systems. *Physica D*, 86:396–427, 1995.

[17] Oleg V. Vasilyev, Yuri Yu Podladchikov, and David a. Yuen. Modeling of compaction driven flow in poro-viscoelastic medium using adaptive wavelet collocation method. *Geophysical Research Letters*, 25(17):3239–3242, 1998.

[18] Oleg V Vasilyev, Yuri Yu Podladchikov, and David A Yuen. Modelling of viscoelastic plume lithosphere interaction using the adaptive multilevel wavelet collocation method. *Geophysical Journal International*, 147(3):579–589, 2001.

[19] Pierre Sagaut, Sebastien Deck, and Marc Terracol. *Multiscale and Multiresolution Approaches in Turbulence*. Imperial College Press, London, 2006.

[20] Daniel E. Goldstein and Oleg V. Vasilyev. Stochastic coherent adaptive large eddy simulation method. *Physics of Fluids*, 16:2497–2513, 2004.

[21] Eric Brown-Dymkoski, Nurlybek Kasimov, and Oleg V. Vasilyev. A characteristic based volume penalization method for general evolution problems applied to compressible viscous flows. *Journal of Computational Physics*, 262:344–357, 2014.

[22] Nicholas K. R. Kevlahan and Oleg V. Vasilyev. An Adaptive Wavelet Collocation Method for Fluid-Structure Interaction at High Reynolds Numbers. *SIAM Journal on Scientific Computing*, 26(6):1894–1915, 2005.

[23] Oleg V. Vasilyev. Solving Multi-dimensional Evolution Problems with Localized Structures using Second Generation Wavelets. *International Journal of Computational Fluid Dynamics*, 17(2):151–168, 2003.

[24] Clayton T. Crowe, John D. Schwarzkopf, Martin Sommerfeld, and Yutaka Tsuji. *Multiphase Flows with Droplets and Particles*. CRC Press, Boca Raton, second edition, 2011.

[25] Guan Heng Yeoh and Jiyuan Tu. *Computational Techniques for Multiphase Flows*. Elsevier, Oxford, 2010.

[26] T B Anderson and R O Y Jackson. A Fluid Mechanical Description of Fluidized Beds. *Industrial & Engineering Chemistry Fundamentals*, 6(4):527–539, 1967.

[27] B.H. Xu and a.B. Yu. Numerical simulation of the gas-solid flow in a fluidized bed by combining discrete particle method with computational fluid dynamics. *Chemical Engineering Science*, 52(16):2785–2809, 1997.

[28] B.P.B. Hoomans, J.a.M. Kuipers, W.J. Briels, and W.P.M. van Swaaij. Discrete particle simulation of bubble and slug formation in a two-dimensional gas-fluidised bed: A hard-sphere approach. *Chemical Engineering Science*, 51(1):99–118, January 1996.

[29] Y. Tsuji, T. Kawaguchi, and T. Tanaka. Discrete particle simulation of two-dimensional fluidized bed. *Powder Technology*, 77:79–87, 1993.

[30] A B Basset. *A treatise on hydrodynamics: with numerous examples.* Deighton Bell, London, 1888.

[31] J Boussinesq. *Theory analytique de la chaleur*, volume 2. L'Ecole Polytechnique, Paris, 1895.

[32] C W Oseen. *Hydrodynamik.* Leipzig, 1927.

[33] Mr R Maxey and Jj J Riley. Equation of motion for a small rigid sphere in a nonuniform flow. *Physics of Fluids*, 26:883, 1983.

[34] A. Ferrante and S. Elghobashi. On the physical mechanisms of two-way coupling in particle-laden isotropic turbulence. *Physics of Fluids*, 15(2003):315–329, 2003.

[35] Q. Wang and K. D. Squires. Large eddy simulation of particle-laden turbulent channel flow. *Physics of Fluids*, 8(1996):1207, 1996.

[36] W Kalthoff, S Schwarzer, and H J Herrmann. Algorithm for the simulation of particle suspensions with inertia effects. *Physical Review E*, 56(2):2234–2242, 1997.

[37] Z. Zhang and a. Prosperetti. A second-order method for three-dimensional particle simulation. *Journal of Computational Physics*, 210:292–324, 2005.

[38] Joseph Feng, Howard H Hu, and Daniel D Joseph. Direct simulation of initial value problems for the motion of solid bodies in a Newtonian fluid. Part 1. Sedimentation. *Journal of Fluid Mechanics*, 261:95–134, 1994.

[39] Zhi Gang Feng and Efstathios E. Michaelides. Heat transfer in particulate flows with Direct Numerical Simulation (DNS). *International Journal of Heat and Mass Transfer*, 52(3-4):777–786, 2009.

[40] Markus Uhlmann. Interface-resolved direct numerical simulation of vertical particulate channel flow in the turbulent regime. *Physics of Fluids*, 20(2008), 2008.

[41] Pierre Jop, Yoël Forterre, and Olivier Pouliquen. A constitutive law for dense granular flows. *Nature*, 441(7094):727–30, June 2006.

[42] Olivier Pouliquen and François Chevoir. Dense flows of dry granular material. *Comptes Rendus Physique*, 3(2):163–175, January 2002.

[43] G D R Midi. On dense granular flows. *The European Physical Journal E*, 14(4):341–65, August 2004.

[44] A Schofield and P Wroth. *Critical State Soil Mechanics*. McGraw-Hill, London, 1968.

[45] R M Nedderman. *Statics and Kinematics of Granular Materials*. Cambridge University Press, Cambridge, 1992.

[46] Charles S Campbell. Rapid Granular Flows. *Annual Review of Fluid Mechanics*, 22:57–92, 1990.

[47] I. Goldhirsch. Scales and kinetics of granular flows. *Chaos*, 9:659–672, 1999.

[48] Colin Denniston and Hao Li. Dynamics and stress in gravity-driven granular flow. *Physical Review E*, 59(3):3289–3292, March 1999.

[49] RM Nedderman and C Laohakul. The thickness of the shear zone of flowing granular materials. *Powder Technology*, 25:91–100, 1980.

[50] O Pouliquen and R Gutfraind. Stress fluctuations and shear zones in quasistatic granular chute flows. *Physical Review E*, 53(1), 1996.

[51] W A Beverloo, H A Leniger, and J van de Velde. The flow of granular solids through orifices. *1Chemical Engineering Science*, 15:260–269, 1961.

[52] Anshu Anand, Jennifer S. Curtis, Carl R. Wassgren, Bruno C. Hancock, and William R. Ketterhagen. Predicting discharge dynamics from a rectangular hopper using the discrete element method (DEM). *Chemical Engineering Science*, 63(24):5821–5830, December 2008.

[53] HE Rose and T Tanaka. Rate of discharge of granular materials from bins and hoppers. *The Engineer*, 208:465–469, 1959.

[54] D Hirshfeld, Y Radzyner, and D C Rapaport. Molecular dynamics studies of granular flow through an aperture. *Physical Review E*, 56(4):4404–4415, 1997.

[55] HM Jaeger and SR Nagel. Physics of the granular state. *Science*, 255(5051):1523–31, March 1992.

[56] Thorsten Pöschel and Thomas Schwager. *Computational Granular Dynamics: Models and Algorithms*. Springer, Berlin, 2005.

[57] J. J Drozd and C Denniston. Simulations of collision times in gravity-driven granular flow. *Europhysics Letters (EPL)*, 76(3):360–366, November 2006.

[58] PA Cundall and ODL Strack. A discrete numerical model for granular assemblies. *Geotechnique*, 29(1):47–65, 1979.

[59] Paul W Cleary and Mark L Sawley. DEM modelling of industrial granular flows: 3D case studies and the effect of particle shape on hopper discharge. *Applied Mathematical Modelling*, 26(2):89–111, February 2002.

[60] J. E. Hilton and P. W. Cleary. Granular flow during hopper discharge. *Physical Review E*, 84(1):011307, July 2011.

[61] N.G. Deen, M. Van Sint Annaland, M.a. Van der Hoef, and J.a.M. Kuipers. Review of discrete particle modeling of fluidized beds. *Chemical Engineering Science*, 62(1-2):28–44, January 2007.

[62] Jesse Capecelatro and Olivier Desjardins. An Euler-Lagrange strategy for simulating particle-laden flows. *Journal of Computational Physics*, 238:1–31, April 2013.

[63] K L Johnson. *Contact Mechanics*. Cambridge University Press, Cambridge, 1989.

[64] J Shäfer, S Dippel, and DE Wolf. Force schemes in simulations of granular materials. *Journal de physique I*, 6:5–20, 1996.

[65] R. Gutfraind and O. Pouliquen. Study of the origin of shear zones in quasi-static vertical chute flows by using discrete particle simulations. *Mechanics of Materials*, 24(4):273–285, December 1996.

[66] H. Kruggel-Emden, S. Wirtz, and V. Scherer. A study on tangential force laws applicable to the discrete element method (DEM) for materials with viscoelastic or plastic behavior. *Chemical Engineering Science*, 63(6):1523–1541, March 2008.

[67] Sudheshna Moka and Prabhu Nott. Statistics of Particle Velocities in Dense Granular Flows. *Physical Review Letters*, 95(6):068003, August 2005.

[68] Shankar Subramaniam. Lagrangian-Eulerian methods for multiphase flows. *Progress in Energy and Combustion Science*, 39:215–245, 2013.

[69] John K. Eaton. Two-way coupled turbulence simulations of gas-particle flows using point-particle tracking. *International Journal of Multiphase Flow*, 35(9):792–800, 2009.

[70] Tristan M. Burton and John K. Eaton. Fully resolved simulations of particle-turbulence interaction. *Journal of Fluid Mechanics*, 545:67–111, 2005.

[71] P. Bagchi and S. Balachandar. Effect of turbulence on the drag and lift of a particle. *Physics of Fluids*, 15(2003):3496–3513, 2003.

[72] Oleg V Vasilyev and Christopher Bowman. Second-Generation Wavelet Collocation Method for the Solution of Partial Differential Equations. *Journal of Computational Physics*, 165:660–693, 2000.

[73] Frank M. White. *Fluid Mechanics.* McGraw-Hill, Boston, fourth edition, 1999.

[74] Wim Sweldens. The Lifting Scheme: A Custom-Design Construction of Biorthogonal Wavelets. *Applied and Computational Harmonic Analysis*, 3:186–200, 1996.

[75] Wim Sweldens. The Lifting Scheme: A Construction of Second Generation Wavelets. *SIAM Journal on Mathematical Analysis*, 29(November):511–546, 1998.

[76] Oleg V. Vasilyev and N. K R Kevlahan. An adaptive multilevel wavelet collocation method for elliptic problems. *Journal of Computational Physics*, 206:412–431, 2005.

[77] David L Donoho. *Interpolating Wavelet Transforms*. Tech. Report 408, Department of Statistics, Stanford University, 1992.

[78] M.P. Allen, D. Frenkel, and J. Talbot. Molecular dynamics simulation using hard particles. *Computer Physics Reports*, 9:301–353, 1989.

[79] William H. Press, Saul A. Teukolsky, William T. Vetterling, and Brian P. Flannery. *Numerical Recipes: The Art of Scientific Computing*. Cambridge University Press, Cambridge, third edition, 2007.

[80] Stuart B. Savage. Gravity flow of cohesionless granular materials in chutes and channels. *Journal of Fluid Mechanics*, 92:53–96, April 1979.

[81] Jaehyuk Choi, Arshad Kudrolli, Rodolfo Rosales, and Martin Bazant. Diffusion and Mixing in Gravity-Driven Dense Granular Flows. *Physical Review Letters*, 92(17):174301, April 2004.

[82] Guoming Hu, Zhenyu Hu, Bin Jian, Liping Liu, and Hui Wan. On the determination of the damping coefficient of non-linear spring-dashpot system to model hertz contact for simulation by discrete element method. *Journal of Computers*, 6(5):984–988, May 2011.

[83] M.A. van der Hoef, M. Ye, M. van Sint Annaland, A.T. Andrews, S. Sundaresan, and J.A.M. Kuipers. Multiscale Modeling of Gas-Fluidized Beds. *Advances in Chemical Engineering*, 31:65–149, 2006.

[84] Samuel F. Foerster, Michel Y. Louge, Hongder Chang, and Khédidja Allia. Measurements of the collision properties of small spheres. *Physics of Fluids*, 6(3):1108, 1994.

[85] P. Gondret, M. Lance, and L. Petit. Bouncing motion of spherical particles in fluids. *Physics of Fluids*, 14(2):643, 2002.

[86] FP Di Maio and A Di Renzo. Analytical solution for the problem of frictional-elastic collisions of spherical particles using the linear model. *Chemical Engineering Science*, 59(16):3461–3475, August 2004.

[87] Meheboob Alam and V. K. Chikkadi. Velocity distribution function and correlations in a granular Poiseuille flow. *Journal of Fluid Mechanics*, 653:175–219, May 2010.

[88] C. Kloss, Christoph Goniva, Alice Hager, Stefan Amberger, and Stefan Pirker. Models , algorithms and validation for opensource DEM and CFD-DEM. *Progress in Computational Fluid Dynamics*, 12:140–152, 2012.

[89] Salvatore Torquato, Thomas M. Truskett, and Pablo G. Debenedetti. Is Random Close Packing of Spheres Well Defined? *Physical Review Letters*, 84(10):2064–2067, 2000.